

ACP-2015-687

Authors' Responses to **Reviewer 1** (anonymous)

Date: 26 February 2016

Title: A numerical study of back-building process in a quasi-stationary rainband with extreme rainfall over northern Taiwan during 11-12 June 2012

Authors: C.-C. Wang, B.-K. Chiou, G. T.-J. Chen, H.-C. Kuo, and C.-H. Liu

1. Overall comments:

The authors present a case study on a heavy precipitation event over northern Taiwan. The case is investigated in reanalysis data, observational data and data from numerical model simulations. The underlying processes of the storm evolution are evaluated, with a special emphasis on the dynamics of the storm. In particular, the developing pressure perturbation is investigated, and its thermodynamic and dynamic contributions are separated. The case is well studied and documented. It could benefit from placing the studied case into a larger context, e.g. by giving an indication, how often these events occur over this area, or by describing if this is a typical or untypical event.

Reply:

The positive views and constructive comments from this reviewer (**Reviewer 1**), as well the comments from the second reviewer, are deeply appreciated, and the paper has been revised according to all these comments and suggestions. In the revised manuscript (color coded), the changes made in response to **Reviewer 1**, **Reviewer 2**, **by ourselves** (mostly minor changes in wording or to correct mistakes), and during the **typesetting** stage of ACPD (to comply with the journal format and style) are marked in **red**, **blue**, **orange**, and **green**, respectively. Thus, words in **green** are the same as seen by the reviewers earlier, and can be ignored. Our reply to the "overall comment" from this reviewer is given in the next paragraph below, while the point-by-point responses to each of the general, minor, and technical comments are listed further below. In each point, how and where the revision is made in the text is specified.

As suggested, the studied case is placed into a larger context, and more material is added to discuss the rarity or unusualness of this event (**p.4, L7-8**), as well as the background forcings from the (Taiwan) topography and the approaching mei-yu front at scales larger than the storm scale (e.g., **p.1, L14-15; p.7, L20-27; p.10, L1-11; p.18, L22-24**). For changes related to the latter point, please also see our reply to the major comment #1 below.

2. General comments:

- 1) In the area where the back-building process occurs, the flow undergoes channeling between the Taiwanese island and the Chinese main land. As described in the study the atmosphere is very moist, especially in the lower layers, thus the channeling leads to strong moisture-flux convergence. In addition, the flow undergoes some lifting over the Taiwanese mountain chain. The fact that LHR and buoyancy play the dominant role in the storm process hints at moisture-flux convergence as the driving mechanism. The process of moisture-flux convergence in a conditionally unstable environment, which naturally leads to the initiation of convection should be mentioned and discussed further.

Reply: At several places (mainly in section 3), the flow splitting due to terrain blocking of Taiwan and the subsequent channeling, convergence, and acceleration (as well as moisture flux convergence) at low levels over the northern Taiwan Strait is discussed with appropriate references (p.1, L14-15; p.7, L20-25; p.8, L4-6; p.10, L1-8; p.12, L14-15 and L18-25). In the revision, it is also stated that such conditions, together with the approaching mei-yu front, are particularly conducive to quasi-linear MCSs, and both the frontal forcing and the terrain-induced (moisture flux) convergence are driving mechanisms at meso- α and meso- β scales in the present case (p.7, L25-27; p.8, L12-15; p.10, L8-11; p.12, L9-10; p.14, L22-25; p.17, L13-15; p.18, L22-23), as suggested.

- 2) The numerical model seems to capture the storm evolution well. However, it appears to me from looking at the figures, that it overestimates the amount of the flow that goes over the mountain chain but underestimates the portion that is directed around the ridge/island and undergoes channeling. As a result, the simulated precipitation tends to occur more on top of the mountains and is underestimated at the tip. Please include some analysis into the manuscript.

Reply: Although our focus of the study is not in the details of flow behavior mentioned by the reviewer here (it would also be very difficult to verify due to sparse coverage of upper-level observations in the mountains and over the ocean around Taiwan), it is stated in the text that the model might somewhat over-estimate the flow over the mountain because it predicted more rainfall in the interior of southern Taiwan than observed, along the lines as suggested (p.9, L17-19, p.11, L19-21).

- 3) The formation mechanism for the layer with negative $\Delta p'$ and negative $\Delta p'_b$

around 5 km between 120.8 and 120.9° remains unclear to me. It coincides with a layer of negative buoyancy. There is no cloud visible, so evaporation of rain can be ruled out.

Reply: While the induced p' and p'_b are more subtle than $\nabla^2 p'_b$ (cf. e.g., Figs. 12g,h and 14d,e), the latter being positive near 120.8°-121°E at 5 km (associated with the development of B2 cell) is apparently due to $\partial B/\partial z > 0$ [or more precisely, $(\rho_0 B)$ becoming less negative with height, cf. e.g., Figs. 13g,h and Eq. (3)]. This is because the adiabatic cooling from rising motion (forced by near-surface convergence) diminishes above 5 km where the atmosphere is potentially stable. The above mechanism is better explained in the revision, as suggested (p.8, L6-8; p.15, L20-23).

- 4) Page 32682, second paragraph: Even though the low levels of the atmosphere are very moist and little rainfall evaporates, downdrafts can still be driven by melting of cold hydrometeors, or simply by buoyancy loading. The buoyancy loading mechanism is studied later in the study. How strong/important is the melting? Melting and evaporation may moreover be quite sensitive to the parametrization of microphysical processes. The study uses a single-moment scheme, which may underestimate the evaporation process, as it cannot reproduce a variable droplet-size distribution (see e.g. Morrison, 2009).

Reply: In the revision, the possible sensitivity of the strength of rear-flank downdraft of B1 on cloud microphysical scheme is noted and the work of Morrison et al. (2009) is cited, as suggested (p.15, L30-31; p.23, L11-13). Nonetheless, at least at later times when the updraft of B1 becomes more tilted and B2 grows higher and stronger (e.g., 2100 UTC, cf. Fig. 13j-l) it would become more difficult for the rear-flank downdraft to reach close to the surface, and this is also pointed out in the revision (p.15, L27-31).

- 5) Mention the term "case study" somewhere.

Reply: While it is quite clear that the present study is on a single event, as indicated throughout the text in the revision (p.1, L19; p.4, L10; p.5, L24; p.7, L11; p.12, L1; p.14, L16; p.16, L23), the term "case study" is explicitly mentioned at several places in the revision (p.1, L16; p.10, L15-16; p.17, L29), as suggested.

- 6) Some of the figures are extremely small and hard to read, especially the labels and land-sea mask. This makes it very difficult to compare the different panels. Please make sure that they are printed larger.

Reply: The contour labels and most of the axis labels in Figs. 10b and 11-16 are all enlarged to improve their readability (p.44-51), and the land/sea boundary in Fig. 4 is also highlighted with thicker outlines (p.29, L16-19; p.36-37), as suggested. Since many figures are arranged (with their panels) to fit a portrait layout, which is used in Atmos. Chem. Phys. (ACP), some of them are not very suited for a landscape layout used during the discussion phase of ACPD. If accepted, the paper will be eventually printed using a portrait layout, and some figures can be printed larger and clearer.

3. Minor comments:

- 1) Page 32680, Line 9: mention already in the abstract which model you are employing.

Reply: The sentence is revised to "...the linear MCS and the BB process in this case are successfully reproduced, and are found to be ...", along the lines as suggested (p.1, L19-20).

- 2) Page 32681, Line 12: clarify what is meant by "slow-moving surface boundary". Is it a front, or a convergence line?

Reply: It is clarified that the boundary can be a front or a convergence line, as suggested (p.2, L19).

- 3) Page 32682, first paragraph: how important are elevated mixed layers remanent from the previous convective events?

Reply: The role of the remnant of elevated mixed-layer is not discussed in these earlier studies, likely because the topography over southern China (hilly terrain) or near Taiwan (offshore with sparse data) is quite different from the Great Plains of the US (flat and quite homogeneous). In the present case, there was little rain over northern Taiwan preceding the current event (and on previous days), and this is noted in the text to indicate that there was no elevated mixed-layer (p.9, L17-20), as suggested.

- 4) Page 32686, line 13: illustrate the "relaxation method further". How is laplace p' inverted to retrieve p ? Which boundary conditions are used?

Reply: An appendix is added to explain the details and the boundary conditions used in the

relaxation method, as suggested (p.6, L22; p.19, L19 to p.20, L23).

- 5) Page 32697: Which diabatic processes are active? Radiative cooling? Or something else?

Reply: The diabatic effects mentioned in section 6 are those associated with phase changes, i.e., condensational heating (from LHR) and evaporative cooling. This is better explained in the revision to avoid confusion, along the lines as suggested (p.16, L14-16).

4. Technical comments:

- 1) Abstract, line 9, replace reproduced with reproduces.

Reply: The sentence is revised to "...the linear MCS and the BB process in the present case are successfully reproduced, and are found to be ..." in response to minor comment #1 (p.1, L19-20).

- 2) Abstract, line 18: replace "gain" with "gained".

Reply: Corrected as suggested (p.1, L28).

- 3) Page 32680, line 24, remove "the" in front of "squall lines".

Reply: Removed as suggested (p.2, L6).

- 4) Page 32681, line 6: replace "potential of" with "potential for".

Reply: Replaced as suggested (p.2, L13).

- 5) Page 32683, line 3: include "whether" or "if" before "some other processes".

Reply: A word "whether" is added, as suggested (p.3, L32).

- 6) Page 32684, line 7-8: Split the sentence up after "numerical simulation".

Reply: The sentence is split into two sentences, as suggested (p.5, L2-4).

- 7) Page 32684, line 23: include "grid points" after 1000 x 800 x 50 and include "as"

before "Already".

Reply: The sentence is revised to "... and a grid dimension (x, y, z) of 1000 × 800 × 50 points (cf. Fig. 1, Table 1). As already described, ..." along the lines as suggested (p.5, L16-17).

8) Page 32685, line 6: replace "on" by "of".

Reply: Replaced as suggested (p.5, L26).

9) Page 32685, equation (1): introduce F_z (presumably turbulent mixing).

Reply: The term F_z is introduced explicitly, as suggested (p.6, L2-3).

10) Page 32688, line 6: include "the level of" before "free convection".

Reply: The sentence is revised to "... to reach the level of free convection at 789 hPa. ...", along the lines as suggested (p.8, L10).

11) Page 32692, line 22: replace "resulted" by "resulting" and remove "the" before "strongest".

Reply: Revised as suggested (p.12, L26-27).

12) Page 32692, line 27: remove "the" before "strongest".

Reply: Removed as suggested (p.12, L31 to p.13, L1).

13) Page 32694, line 26-27: this sentence is confusing. Rewrite. The dominant contributor is p_b .

Reply: The sentence is rewritten to "...the total pattern of $\nabla^2 p$ is dominated by $\nabla^2 p_b$ ' everywhere, except near the based of B1 (below 1.5 km) where $\nabla^2 p_d$ ' contributes significantly (Fig. 12k and l). ..." for better clarity, as suggested (p.14, L20-22).

References:

H. Morrison, G. Thompson, and V. Tatarskii, 2009: Impact of Cloud Microphysics on the Development of Trailing Stratiform Precipitation in a Simulated Squall Line:

Comparison of One- and Two-Moment Schemes. Mon. Wea. Rev., 137,
991-1007. doi: <http://dx.doi.org/10.1175/2008MWR2556.1>

ACP-2015-687

Authors' Responses to [Reviewer 2](#) (anonymous)

Date: 26 February 2016

Title: A numerical study of back-building process in a quasi-stationary rainband with extreme rainfall over northern Taiwan during 11-12 June 2012

Authors: C.-C. Wang, B.-K. Chiou, G. T.-J. Chen, H.-C. Kuo, and C.-H. Liu

1. General comment:

With a cloud-resolving model, this study investigates a quasi-stationary rainband that caused extreme rainfall over northern Taiwan, in an attempt to understand the processes responsible for the occurrence of severe flooding associated with this particular case. A primary conclusion drawn in this article is that the back-building (BB) processes were suggested to be crucial for contributing to the occurrence of the observed extreme rainfall. Some modeling aspects implicit in the BB processes are also presented and discussed. The central theme of the study is generally interesting. Unfortunately, the reliability of the conclusions learned from the study suffers from a number of fundamental problems, which can be clearly seen based on the current form of the manuscript. The reviewer believe that a significant re-work on writing and analysis will be required to accommodate these serious concerns and the resultant manuscript would be very different from this one.

Reply:

The comments from this reviewer ([Reviewer 2](#)), as well as those from [Reviewer 1](#), are all appreciated, and the paper has been revised according to all these comments and suggestions. In the revised manuscript (color coded), the changes made in response to [Reviewer 1](#), [Reviewer 2](#), [by ourselves](#) (mostly minor changes in wording or to correct mistakes), and during the [typesetting](#) stage of ACPD (to comply with the journal format and style) are marked in [red](#), [blue](#), [orange](#), and [green](#), respectively. Thus, words in [green](#) are the same as seen by the reviewers earlier, and can be ignored. Our reply to the “general comment” from this reviewer is given in the next paragraph below, while the point-by-point responses to each of the specific comments are listed further below. In each point, how and where the revision is made in the text is indicated.

In response to the overall comment from this review, revision is made mainly to (1) replace Fig. 6 with a new figure, which can more clearly depict the BB process at the end of the convective line and/or to the west of old cells, and (2) to clarify that there are other important processes leading to the formation of the quasi-linear MCS beyond the storm scale

(such as frontal and terrain forcings), but we have focused on the BB process west of old cells inside the line on the convective scale (meso- γ) in the present study. As we know, in extreme events such as the present case, there are often several factors and forcings working in synergy across a wide range of scales to lead to their occurrence. Thus, each of these factors and the interactions among them, in our opinion, is worthwhile to investigate. In the present case, the larger-scale forcings (at meso- β scale and larger) provided the background to the problem of our focus, and we have clarified this point in the revision where appropriate (e.g., p.7, L25-27; p.8, L12-15; p.10, L2-11; p.12, L9-10; p.18, L22-23). Please also see our more-detailed reply to each of the specific comments below.

2. Specific comments:

1. Various observations and modeling results presented in the paper did support a close relevance of the frontal forcings to the development of heavy rainfall associated with the studied rainband. For example, the CWB surface analysis, the NCEP analysis, and the ASCAT winds shown in Figs. 1 and 2a,c,e all indicate that a slow-moving Meiyu front was oriented NE-SW (roughly along 25 N) and located immediately north of Taiwan. The Mei-yu front coincided very well with the elongated studied rainband, and the orientation and spatial scale for the front and the rainband were consistent with each other, as illustrated by radar maps in Fig. 4. These observations strongly suggest that the convective system causing severe floods over northern Taiwan actually was a frontal rainband rather than a pre-frontal squall line as claimed by the authors. The convective forcings associated with the frontal zone are expected to be one of the primary contributors but were completely ignored in the current context of this study.

Reply:

We agree with the reviewer that the forcing associated with the approaching front was an important contributor to the development of the quasi-linear MCSs in the present event, and we do not intent to deny its importance, not even in our previous draft. As suggested by this reviewer, to better place our current study into its context, we have added more material to discuss the role of the approaching mei-yu front (the frontal forcing) and the flow splitting and subsequent channeling, convergence, and acceleration (the topographic forcing) at low levels over the northern Taiwan Strait with appropriate references in the revision (p.1, L14-15; p.4, L10-12; p.7, L20-27; p.10, L1-6; p.12, L18-21). It is stated that such conditions are particularly conducive to quasi-linear MCSs, and both the frontal forcing and the terrain-induced convergence are driving mechanisms at meso- α and meso- β scales in the present case (p.7, L25-27; p.8, L12-15; p.10, L8-11; p.12, L9-10; p.16, L20-21; p.18, L22-23;

p.22, L19-21), as suggested. It is also better clarified that the focus of the study is on new cell initiation at convective scale under the frontal and topographic forcings beyond the storm scale (p.4, L10-12; p.10, L12-17; p.18, L24).

2. Further support of the reviewer's point mentioned in the comment #1 is provided by the CReSS model simulations presented in Fig. 7, which shows that the studied rainband formed over northern Taiwan was collocated with a narrow confluent zone in the vicinity of the Mei-yu front between northeasterlies and southwesterlies (cf. Fig. 7f). Note also that an additional wind shift zone was evident offshore over northwestern and northeastern Taiwan (Fig. 7), presumably due to the common occurrence of orographic blocking and/or the leeside effects of topography as prevailing southwesterly flow interacts with Taiwan island during the Mei-yu season (e.g., Sun et al. 1991, MWR; Chen and Li 1995, MWR; Li and Chen 1998, MWR; Yeh and Chen 2002, MWR). This topographically generated convergence may represent another critical mesoscale forcing, favoring the development and organization of deep moist convection associated with the studied rainband.

It is clear that both observations and modeling results provide consistent evidences that the organization and maintenance of the studied rainband are closely related to the frontal and topographic forcings. In fact, the authors have also admitted in the manuscript that the development of the studied precipitation system is closely tied to the low-level convergence associated with the frontal forcing (e.g., L26-29 in P32689). Given this fact, it is not wise to downplay the roles of the frontal forcing in contributing to the occurrence of the observed heavy rainfall.

Reply:

Similar to our reply to the specific comment #1 above, we agree with the reviewer that the forcing induced by the blocking effect of Taiwan topography (upstream flow splitting and subsequent channeling, convergence, and acceleration and the LLJ) at low levels over the northern Taiwan Strait was also an important factor and is responsible for the formation of the second quasi-linear MCS during 1800-2400 UTC in our model simulation (according to Figs. 4 and 7, with surface frontal positions marked when available, see the text in 2nd paragraph, p.11, p.36-37, p.40-41). In the revision, the role of topographic forcing is also discussed with appropriate references, as suggested (p.7, L20-27; p.8, L4-6; p.8, L12-15; p.12, L18-21), as we have no intention to downplay its possible role. Again, it is also better clarified that the focus of the study is aimed at the new cell initiation at convective scale, under the frontal and topographic forcings at larger scales beyond the storm scale (p.4, L10-12; p.10, L1-6 and L8-17; p.12, L9-10; p.18, L22-24).

3. The authors strongly argue that the BB processes are a key mechanism for the generation of the convective system that caused severe floods over northern Taiwan. However, this is obviously not the case, as indicated in the sequence of radar maps presented in Fig. 6. Based on these radar-observed precipitation signatures, severe floods over northern Taiwan could be mostly attributed to the presence of an approximately W-E elongated, quasi-stationary rainband. Several precipitation cells (Fig. 6) were formed near the western end of the studied rainband, as claimed by the authors, but they were quite transient and were generally located well offshore, far away from the target area of heaviest rainfall over northern Taiwan. In contrast, most of new precipitation cells conducive to the maintenance of the rainband's convection over land were evidently produced immediately ahead (south) of the entire length of the rainband (i.e., the inflow side), particularly for the inland region of northern Taiwan (cf. Figs. 6i-m). These cells were oriented (organized) roughly parallel to the preexisting rainband. In addition, the enhanced precipitation of the rainband tended to exhibit a quasi-steady signature (Fig. 6), which is in turn consistent with the influence of a persistent convective forcing associated with the slow-moving Mei-yu front as described in the comment#1 and #2. These observational evidences regarding the rainband's evolution did not support the likelihood that the BB processes are a reasonable scenario considering the extreme rainfall observed over northern Taiwan.

Reply:

In the revision, Fig. 6 in the previous draft is replaced by a new set of panels using a different color scale, which can better depict the convective elements embedded inside the line and thus their evolution (e.g., new initiation and merging), and this new figure can more clearly show the BB process do take place at the end of the convective line as well as to the west of old cells in the present event (p.18, L13 and L28; p.29, L25-28; p.39). In the text, it is also better conveyed that (1) they were clear westward extension of the linear MCS (as shown in Figs. 4 and 6; p.36, p.39), i.e., the back-building behavior clearly significantly lengthened the heavy-rainfall period (since most cells at/near the western end of the line, transient or otherwise, eventually moves onshore to cause rainfall over land) (evident in Fig. 6; p.8, L27-30; p.9, L29-32; p.10, L11-12; p.39), and (2) some of the new cells just west of old cells in Fig. 6 formed close to the land, and as their counterpart in the model, the studied new cell does merge with the old cell and produce rainfall at high intensity over northern Taiwan (cf. Figs. 7f and 9, p.9, L24, L27; p.11, L26-30). So, as one of the factors, the BB process at the cloud scale indeed contributed to the heavy rainfall in northern Taiwan in the present case (as in many other cases throughout the world), whereas the frontal and topographic forcings are also important factors acting at larger scale, as clarified above and in the revision (p.1, L14-15;

p.4, L10; p.8, L12-15; p.10, 1-6 and L8-11; p.12, L9-10; p.18, L7). In addition, the structure of multiple lines, as mentioned by this reviewer, is noted with appropriate references on its possible mechanism cited in the revision (p.10, L6-8; p.22, L1-2; p.26, L25-26).

4. Suggestion: Because the scientific objective of the study is to understand the processes leading to the extreme rainfall for this particular event, the reviewer strongly feel that the authors should consider focusing on other observational aspects that are more relevant to the occurrence of heavy rainfall, instead of sticking to the unsupported mechanism (i.e., the BB process). For example, relative importance of frontal and topographic forcings and their roles in triggering and organizing the precipitation rainbands observed over northern Taiwan may be worth pursuing further to provide more solid and convincing descriptions.

Reply:

In our previous as well as the revised draft, it is explicitly stated that the BB process, and more specifically, why the location about 15-30 km upstream from old cells is more favorable for the initiation of new BB cells (as seen in observations and our model simulation) are the objective, or the scientific question that we wish to address in this study (p.3, L32 to p.4, L2; p.4, L10-12; p.10, L11-17). Thus, the problem to be studied is at convective scale and our goal is not to identify or study the “most important” factor or process leading to the heavy rainfall in northern Taiwan (e.g., p.10, L11-17), which seems to be the purpose interpreted by this reviewer. In the revision, as mentioned above, we have clarified this point and also noted the importance of the processes identified by this reviewer (i.e., the frontal and topographic forcings at scales beyond the storm scale) in the text where appropriate (p.1, L14-15; p.4, L10; p.10, L1-6 and L8-11; p.12, L9-10; p.16, L20-21; p.17, L13-15; p.18, L22-24). As for the suggestion, one of our current studies with a graduate student is focused on the synoptic evolution leading to the event throughout 10-12 June 2012, and this study will most likely touch upon those aspects mentioned by this reviewer that are also important to the occurrence of heavy rainfall. However, that study will indeed be very different from the present one due to their different focuses.

A numerical study of back-building process in a quasi-stationary rainband with extreme rainfall over northern Taiwan during 11-12 June 2012

C.-C. Wang¹, B.-K. Chiou¹, G. T.-J. Chen², H.-C. Kuo², and C.-H. Liu³

¹ Department of Earth Sciences, National Taiwan Normal University, Taipei, Taiwan

² Department of Atmospheric Sciences, National Taiwan University, Taipei, Taiwan

³ Department of Atmospheric Sciences, Chinese Culture University, Taipei, Taiwan

Correspondence to: C.-C. Wang (cwang@ntnu.edu.tw)

Abstract

During 11-12 June 2012, quasi-stationary linear mesoscale convective systems (MCSs) developed near northern Taiwan and produced extreme rainfall up to 510 mm and severe flooding in Taipei. Among other factors across the scale, the back-building (BB) process in these MCSs contributed to the extreme rainfall and thus is investigated using a cloud-resolving model in the case study here. Specifically, we seek answers to the question why the location about 15-30 km upstream from the old cell is often more favorable for new cell initiation without the cold pool mechanism in this subtropical event during the mei-yu season.

With a horizontal grid size of 1.5 km, the linear MCS and the BB process in this case are successfully reproduced, and are found to be influenced more by the thermodynamic and less by dynamic effects. During initiation in a background with convective instability, new cells are associated with positive (negative) buoyancy below (above) due to latent heating (adiabatic cooling), which represent a gradual destabilization. At the beginning, the new development is close to the old convection, which provides stronger warming below and additional cooling at mid-levels from evaporation of condensates in the downdraft at the rear flank, thus yielding a more rapid destabilization. This enhanced upward decrease in buoyancy at low levels eventually creates an upward perturbation pressure gradient force to drive further development along with the positive buoyancy itself. After the new cell has gained sufficient

1 strength, the old cell's rear-flank downdraft also acts to separate the new cell to about 20 km
2 upstream. Therefore, the advantages of the spot in the BB process can be explained.

3

4 **1 Introduction**

5 As a common type of mesoscale convective systems (MCSs) with a lifespan around 3-12 h,
6 organized rainbands such as squall lines are capable of producing persistent precipitation at
7 high intensity, compared to ordinary, isolated, or scattered convection (e.g., Carbone, 1982;
8 Bluestein and Jain, 1985; Rotunno et al., 1988; Browning, 1990; Houze et al., 1990; Chen and
9 Chou, 1993; LeMone et al., 1998; Parker and Johnson, 2000; Doswell, 2001; Johnson and
10 Mapes, 2001; Sun and Lee, 2002; Weisman and Rotunno, 2004; Meng et al., 2013). When
11 such rainbands are slow-moving and the embedded deep convective cells travel at small
12 angles almost parallel to the line, multiple cells can pass through the same locations in
13 succession to rapidly increase rainfall accumulation and the potential for flash floods (e.g.,
14 Maddox et al., 1979; Doswell et al., 1996; Brooks and Stensrud, 2000; Parker and Johnson,
15 2004). For the eastern two thirds of the United States, Schumacher and Johnson (2005, 2006)
16 found that 66% of extreme rainfall events there are caused by quasi-linear MCSs, among
17 which 54% are produced by only two modes in organization. The training line-adjointing
18 stratiform (TL/AS) type often forms along (or north of) an east-west (E-W) aligned, pre-
19 existing slow-moving surface boundary (such as a front or a convergence line), and a series of
20 embedded "training" cells move eastward (also Stevenson and Schumacher, 2014; Peters and
21 Roebber, 2014; Peters and Schumacher, 2015). The second type is quasi-stationary back-
22 building (BB) systems, which depend more on meso- and storm-scale forcing and processes.
23 In BB lines, new cells form repeatedly on the upwind side at nearly the same location then
24 move downstream, making the line as a whole almost stationary (also Chappell, 1986; Corfidi
25 et al., 1996). Compared to the TL/AS type, the BB systems are smaller and more localized,
26 and thus more difficult to predict (e.g., Schumacher and Johnson, 2005).

27 To repeatedly trigger new cells in BB MCSs at mid-latitudes, a well-known mechanism is
28 through convectively-generated outflow boundary from downdrafts, i.e., at the leading edge
29 of the cold pool (or the gust front) that extends into the upwind side (e.g., Doswell et al., 1996;
30 Parker and Johnson, 2000; Corfidi, 2003; Schumacher and Johnson, 2005, 2009; Houston and
31 Wilhelmson, 2007; Moore et al., 2012). Similar mechanisms for the BB process are also
32 found in some events in the East Asia (e.g., H. Wang et al., 2014; Jeong et al., 2015).

1 However, toward lower latitudes such as the subtropics and tropics, the environments may be
2 less conducive to cold pool development (e.g., Tompkins, 2001). Some studies on extreme
3 rainfall events in South China and Taiwan have shown that surface-based cold air produced
4 by previous convection that had dissipated for hours or even in the day before, when
5 impinged by the moist monsoonal flow, in particular the low-level jet (LLJ), can act to trigger
6 new convection in succession (e.g., Zhang and Zhang, 2012; Xu et al., 2012; C.-C. Wang et
7 al., 2014a; Luo et al., 2014). Such mechanisms by “cold domes,” however, are different from
8 the lifting at gust fronts produced by coexisting, dissipating cells or those that had just
9 dissipated, and the induced MCSs may be less organized if a linear forcing such as a front or
10 low-level convergence zone is absent (e.g., Xu et al., 2012; C.-C. Wang et al., 2014b).

11 Even though the environments near Taiwan (and some other subtropical regions) typically are
12 not favorable for strong cold pools mainly due to high moisture content at low levels (e.g.,
13 Tompkins, 2001; James and Markowski, 2010; Yu and Chen, 2011) as mentioned, BB MCSs
14 are still found (e.g., Li et al., 1997). For these systems, the mechanism for upstream initiation
15 of new cells at the end of the convective line, presumably also dominated by storm-scale
16 processes as their US counterparts (Schumacher and Johnson, 2005), is not clear. Recently,
17 the roles of pressure perturbation (p'), in particular the dynamical pressure perturbation (p'_d ,
18 e.g., Rotunno and Klemp, 1982; Weisman and Klemp, 1986; Klemp, 1987, and many others),
19 in the evolution of convective cells inside the E-W BB rainbands associated with Typhoon
20 Morakot (2009) and extreme rainfall (e.g., Wang et al., 2012) are examined by Wang et al.
21 (2015, hereafter referred to as WKJ15). They found that in the presence of an intense westerly
22 LLJ, the interaction between updraft and vertical wind shear (e.g., Klemp, 1987) induces
23 positive (negative) p'_d at the western (eastern) flank of the updraft below the jet-core level
24 (with westerly shear) but a reversed pattern above (with easterly shear), and thus an upward-
25 directed perturbation pressure gradient force (PGF) at the western (rear) flank (see e.g., Fig. 6
26 of WKJ15). This leads to a slow-down in the propagation speed of mature cells and promotes
27 cell merger inside the rainbands, as often observed in quasi-linear multi-cell MCSs. A
28 reduced speed of old cell and positive p'_d at its rear flank near the surface can also enhance
29 convergence and contribute to upstream new cell initiation without the cold pool (WKJ15).
30 Obviously, one question worth exploring is whether a mechanism similar to the Morakot case
31 also plays an important role in other BB rainbands near Taiwan with the presence of a LLJ,
32 for example, those during the mei-yu season (May-June), or whether some other processes are

1 also involved? Thus, we seek to further **understand and** clarify the details of the BB process in
2 the case below.

3 During 11-12 June 2012, both TL/AS and BB MCSs developed in succession near northern
4 Taiwan, and produced extreme rainfall up to 510 mm overnight (roughly during 14:00-24:00
5 UTC 11 June, where LST = UTC + 8 h), in Taipei City and the surrounding metropolitan area.
6 Many densely-populated urban regions were flooded, and one day (12 June) was declared off
7 work in Taipei, the first ever in Taiwan in mei-yu season due to heavy rainfall. **Thus, this**
8 **extreme-rainfall event was rare in its total amount, duration, and location.** As will be shown
9 later, clear BB behavior occurred in the quasi-stationary MCSs and contributed to the extreme
10 rainfall in northern Taiwan in this event, **among other factors across the scale.** Thus, this case
11 is studied herein for details in the BB process **at the convective scale,** mainly through
12 numerical simulation using a cloud-resolving model at a horizontal grid size of 1.5 km. Below,
13 the data used and the methodology employed are described in **Sect. 2,** and the extreme rainfall
14 event of 11-12 June 2012, including its synoptic environment, are overviewed in **Sect. 3.** In
15 **Sect. 4,** our simulation results are validated against observations, and further used to
16 investigate the BB process upstream from the old cells. This evolution is then compared with
17 the initiation of an isolated cell in **Sect. 5** to identify the important factors in the BB process,
18 and finally the conclusion and summary of this work are given in **Sect. 6.**

19

20 **2 Data and methodology**

21 **2.1 Observational data**

22 In this study, the data used include weather maps from the Central Weather Bureau (CWB) of
23 Taiwan and gridded final analyses ($0.5^\circ \times 0.5^\circ$, every 6 h) from the National Center for
24 Environmental Prediction (NCEP) at 26 levels from 1000 to 10 hPa (including the surface
25 level) covering the case period. The space-borne Advanced Scatterometer (ASCAT)
26 observations are also used to assist the analysis of frontal position. For conditions in the pre-
27 storm environment, the sounding at Panchiao (near Taipei City) is used. For the evolution of
28 the MCS and the resulted rainfall, the vertical maximum indicator (VMI) composites of radar
29 reflectivity and hourly data from the rain-gauge network (Hsu, 1998) in Taiwan, both
30 provided by the CWB, are employed. The above observational data are used both for analysis
31 and verification of model results.

1 2.2 The CReSS model and experiment

2 The Cloud-Resolving Storm Simulator (CReSS) is used for our numerical simulation. It is a
3 cloud-resolving model that employs a nonhydrostatic and compressible equation set and a
4 height-based terrain-following vertical coordinate (Tsuboki and Sakakibara, 2002, 2007).
5 Clouds are treated explicitly in CReSS using a bulk cold-rain microphysical scheme (Lin et
6 al., 1983; Cotton et al., 1986; Murakami, 1990; Ikawa and Saito, 1991; Murakami et al., 1994)
7 with a total of six species (vapor, cloud water, cloud ice, rain, snow, and graupel). Sub-grid
8 scale processes parameterized include turbulent mixing in the planetary boundary layer (PBL),
9 radiation, and surface momentum and energy fluxes (Kondo, 1976; Louis et al., 1981; Segami
10 et al., 1989). With a single domain (no nesting), this model has been used to study a number
11 of heavy-rainfall events around Taiwan during the mei-yu season (e.g., C.-C. Wang et al.,
12 2005, 2011, 2014a,b; Wang and Huang, 2009) as well as for real-time forecasts (e.g., Wang et
13 al., 2013, 2016; Wang, 2015). The CReSS model is open to the research community upon
14 request, and its further details can be found in the works referenced above and at
15 http://www.rain.hyarc.nagoya-u.ac.jp/~tsuboki/cress_html/index_cress_jpn.html.

16 In this study, the simulation is performed using a horizontal grid spacing of 1.5 km and a grid
17 dimension (x, y, z) of 1000 × 800 × 50 points (cf. Fig. 1, Table 1). As already described, the
18 NCEP 0.5° × 0.5° gridded final analyses serve as the initial and boundary conditions (IC/BCs)
19 of the model run from 12:00 UTC 10 June to 12:00 UTC 12 June 2012 (for 48 h). At the
20 lower boundary, real terrain at 30 s resolution (or (1/120)°, roughly 900 m) and observed
21 weekly sea surface temperature (SST, Reynolds et al., 2002) are provided. The model
22 configuration and major aspects of the experiment are summarized in Table 1.

23 2.3 Analysis of vertical momentum and pressure perturbations

24 To investigate the BB process taking place in the present case using model outputs, the
25 methods below, following Wilhelmson and Ogura (1972), Rotunno and Klemp (1982), Klemp
26 (1987), and Parker and Johnson (2004), are used to perform analysis of vertical momentum
27 and pressure perturbations. With the background environment assumed to be in hydrostatic
28 equilibrium, the vertical momentum equation can be written as

$$29 \frac{dw}{dt} = -\frac{1}{\rho} \frac{\partial p'}{\partial z} - \frac{\rho'}{\rho} g + F_z \approx -\frac{1}{\rho_0} \frac{\partial p'}{\partial z} - \frac{\rho'}{\rho_0} g + F_z \quad (1)$$

1 where all variables have their conventional meanings. Here, $\rho = \rho_0 + \rho'$, where ρ_0 is the
 2 background value and ρ' the perturbation part of ρ , $B = -g(\rho'/\rho_0)$ is the buoyancy, and F_z is
 3 the friction term by turbulent mixing. Thus, the vertical acceleration is driven by an imbalance
 4 among the perturbation PGF, buoyancy, and turbulent mixing. The buoyancy is constituted by
 5 the gaseous effect and the drag of all condensates, and can be expressed as

$$6 \quad B = -\frac{\rho'}{\rho_0} g = g \frac{\theta'_v}{\theta_{v0}} - g \sum q_x \quad (2)$$

7 where θ_v is the virtual potential temperature (and $\theta_v = \theta_{v0} + \theta'_v$) and its perturbation accounts
 8 for the gaseous effect, while q_x denotes the mixing ratio of any condensate species.

9 The perturbation pressure p' can be divided into the dynamical and buoyant components as p'
 10 $= p'_d + p'_b$, and the diagnostic pressure equations for the anelastic set, with friction omitted
 11 (e.g., Rotunno and Klemp, 1982; Parker and Johnson, 2004), are

$$12 \quad \nabla^2 p'_b = \frac{\partial}{\partial z} (\rho_0 B) \quad \text{and} \quad (3)$$

$$13 \quad \nabla^2 p'_d = -\rho_0 \left[\left(\frac{\partial u}{\partial x} \right)^2 + \left(\frac{\partial v}{\partial y} \right)^2 + \left(\frac{\partial w}{\partial z} \right)^2 - w^2 \frac{\partial^2}{\partial z^2} (\ln \rho_0) \right] - 2\rho_0 \left(\frac{\partial v}{\partial x} \frac{\partial u}{\partial y} + \frac{\partial u}{\partial z} \frac{\partial w}{\partial x} + \frac{\partial v}{\partial z} \frac{\partial w}{\partial y} \right) \quad (4)$$

14 where ∇^2 is the laplacian operator. In both equations, a maximum (minimum) in $\nabla^2 p'$
 15 corresponds to a minimum (maximum) in p' itself. Equation (3) states that p'_b is related to the
 16 vertical gradient of the product of ρ_0 and B . On the RHS of Eq. (4), inside the brackets are
 17 extension terms which imply maximized p'_d in regions of nonzero divergence or deformation.
 18 The other terms inside the parentheses are shearing terms and imply minimized p'_d in regions
 19 of nonzero vorticity (Parker and Johnson, 2004). The shearing effects include those related to
 20 vertical wind shear ($\partial u/\partial z$ and $\partial v/\partial z$) associated with the LLJ, as reviewed in Sect. 1 for the
 21 Morakot case. After $\nabla^2 p'_b$ or $\nabla^2 p'_d$ is obtained from Eqs. (3) or (4), the relaxation method is
 22 used to solve the associated pressure perturbation through iteration (see Appendix for details).

23 To provide additional verification, a second, independent method is also used in this study to
 24 compute p' as in WKJ15. In this method, p' is separated from its background pressure (p_0),
 25 defined as

$$26 \quad p_0(x, y, z, t) = \langle p \rangle(x, y, z) + \Delta p(z, t), \quad (5)$$

1 where $\langle p \rangle$ is the time-averaged pressure over a fixed period, and Δp is the deviation of the
2 areal-mean pressure \bar{p} at any given instant from its time mean $\langle \bar{p} \rangle$, such that

$$3 \quad \Delta p(z, t) = \bar{p}(z, t) - \langle \bar{p} \rangle(z). \quad (6)$$

4 Thus, the gradual decrease of the areal-mean pressure with time as the mei-yu front
5 approaches from the north is reflected in Δp , and taken into account in p_0 besides the spatial
6 variation in mean (time-averaged) p [cf. Eq. (5)]. Then, p' is computed simply as

$$7 \quad p'(x, y, z, t) = p(x, y, z, t) - p_0(x, y, z, t). \quad (7)$$

8 Referred to as the separation method, it is also applied to other variables to separate the
9 perturbation and the background where needed, such as for ρ and θ_v in Eqs. (1) and (2).

10

11 **3 Case overview**

12 **3.1 Synoptic and storm environment**

13 In this section, the synoptic conditions and the BB rainbands responsible for the extreme
14 rainfall are described. Figure 1 shows the surface weather map at 12:00 UTC 11 June 2012,
15 about 2 h before heavy rainfall started in northern Taiwan. Extending from the East China Sea
16 to southern China (ENE-WSW), the mei-yu front was about 130 km north of Taiwan, with
17 almost an upright structure up to 700 hPa in the area. The frontal position at this time is in
18 agreement with the NCEP analysis at 950 hPa (Fig. 2a), which also reveals the strong
19 southwesterly LLJ south of the front over the Taiwan Strait and off southeastern Taiwan, as
20 well as the ASCAT observation at 13:00 UTC (Fig. 2e). While the LLJ reaches 20 m s⁻¹ in
21 maximum speed (at 950 hPa), the axis over the strait points toward northwestern Taiwan
22 between the front and the island's topography (Fig. 2a). Such a configuration is produced in
23 response to flow splitting due to terrain blocking and the subsequent channeling, convergence,
24 and acceleration (as well as moisture flux convergence) at low levels over the northern
25 Taiwan Strait (e.g., Li and Chen, 1998; Chen et al., 2005), and is particularly conducive to
26 quasi-linear MCSs with the approaching mei-yu front (e.g., Yeh and Chen, 2002; Wang et al.,
27 2005). The NCEP analyses every 6 h shows that the 950-hPa front reached northern Taiwan
28 near 00:00 UTC 12 June (Fig. 2c), also consistent with ASCAT data at 02:00 UTC (Fig. 2f).
29 Afterward, the mei-yu front advanced rapidly across Taiwan and reached about 23°N within 6

1 h (Fig. 2c), as the rainfall in northern Taiwan gradually weakened (cf. Fig. 8, to be discussed
2 later).

3 The Panchiao sounding (Fig. 3) in the Taipei metropolitan area (cf. Fig. 2c) at 12:00 UTC 11
4 June indicated very strong southwesterly flow throughout the lower troposphere, with a peak
5 of 25 m s^{-1} near 925 hPa and a well-mixed temperature profile underneath, consistent with the
6 barrier jet (e.g., Li and Chen, 1998; Chen et al., 2005). The temperature lapse rate below
7 about 550 hPa was mostly between the dry and moist adiabats, indicating conditional
8 instability. The convective available potential energy (CAPE) was 583 J kg^{-1} and sufficient to
9 support deep convection, if the air parcel could overcome the convective inhibition (CIN) of
10 78 J kg^{-1} to reach the level of free convection at 789 hPa. Obviously, these conditions were
11 soon met since heavy rainfall did occur in Taipei. Note also that the humidity was quite high
12 below about 550 hPa, and a dry layer did not exist throughout the troposphere. Thus, with
13 instability and low-level convergence, the strong, deep, and moisture-laden southwesterly
14 flow near and to the south of the approaching mei-yu front was clearly very favorable for
15 active convection and substantial rainfall (e.g., Jou and Deng, 1992; C.-C. Wang et al., 2014a).

16 3.2 The back-building rainband with extreme rainfall

17 Figure 4 presents the composite VMI radar reflectivity from the ground-based radars in
18 Taiwan at 1 h intervals, and depicts the evolution of the rainbands causing the extreme rainfall
19 in northern Taiwan. At 12:00 UTC 11 June (Fig. 4a), an intense ENE-WSW-oriented squall
20 line, with peak reflectivity in convective elements $\geq 50 \text{ dBZ}$, already formed and was
21 approaching northern Taiwan to within about 30 km, i.e., at some 80-100 km ahead of the
22 surface mei-yu front (cf. Figs. 1 and 2a). With a bulging middle section and trailing stratiform,
23 the squall line moved southward at about 15 km h^{-1} and into northern Taiwan by 14:00 UTC
24 (Fig. 4b and c). During the following hours through 18:00 UTC, this squall line continued to
25 advance slowly and into 25°N , so that much of the northern Taiwan was covered by echoes
26 with high reflectivity (Fig. 4d-g), while the stratiform region gradually moved eastward, in
27 agreement with the upper-level wind (cf. Fig. 3). After 18:00 UTC, the convection through
28 northern Taiwan evolved into a narrow line that remained quasi-stationary for hours until
29 23:00 UTC (Fig. 4g-l), with evident new development, i.e., back-building behavior, toward
30 the west (to be detailed later). Eventually, this linear MCS started to move south slowly and
31 gradually away from the Taipei area after 00:00 UTC 12 June (Fig. 4m-o), likely in

1 conjunction with the surface front with the arrival of the northeasterly flow (cf. Fig. 2c and f).
2 During the entire period of Fig. 4, the mountain interiors in central and southern Taiwan also
3 received continuous rainfall from forced uplift of the strong LLJ by the topography (cf. Fig.
4 2a and c), and another squall line also approached southern Taiwan from the west and made
5 landfall near 22:00 UTC 11 June (Fig. 4i-o). Nonetheless, the reflectivity over northern
6 Taiwan was both very active and lengthy, and produced by two types of MCSs: the first was
7 the squall line before 18:00 UTC 11 June and reminiscent to a TL/AS system, and the second
8 was the quasi-stationary BB MCS after 18:00 UTC (Fig. 4).

9 The distributions of 6 h accumulated rainfall during 12:00-18:00 and 18:00-24:00 UTC 11
10 June are shown in Fig. 5a and b. While three distinct rainfall centers over northern, central,
11 and southern Taiwan were produced in each period, the amount over northern Taiwan was the
12 highest. The rainfall during 12:00-18:00 UTC was maximized along the northwestern coast
13 and decreased inland (Fig. 5a), consistent with the MCS that moved in from the ocean (cf. Fig.
14 4). On the other hand, the rainfall was more concentrated during 18:00-24:00 UTC with
15 almost an E-W alignment, and the center was right near the Taipei City (Fig. 5b). The peak
16 amount during this later 6 h period was 311 mm, and an extreme value of 510 mm was
17 recorded overnight from the entire event. It is perhaps worthy to note that the mountainous
18 interior in central and southern Taiwan also received heavy rainfall since about 00:00 UTC 10
19 June (presumably due to forced uplift), but little rain fell over northern Taiwan prior to the
20 current event.

21 While some BB behavior also occurred in the TL/AS-type squall line, it was more active in
22 the quasi-stationary BB system after 18:00 UTC and can be well depicted by the radar VMI
23 reflectivity every 10 min (Fig. 6). As marked by the short arrows, frequent BB activities can
24 be spotted at the western end of the convective line or west of existing mature cells, and some
25 of them were quite close to the northwestern coast of Taiwan. After formation, they moved at
26 small angles from the ENE-WSW-oriented quasi-stationary line, repeatedly across northern
27 Taiwan with frequent cell mergers similar to those in WKJ15 (Fig. 6). The resulted rainfall in
28 Fig. 5b, with the maximum located inland near Taipei, also implies that many cells matured
29 after they moved onshore instead of over the ocean prior to landfall. Since the length of the
30 line with active cells upstream from Taipei is about 160 km and most cells travelled at the
31 speed range of 60-80 km h⁻¹ in Fig. 6, the heavy rainfall would last only 2-2.5 h and much
32 shorter than in reality (cf. Fig. 5), if there were no new developments westward along the line.

1 In extreme events such as the present one, there are often several factors and forcings working
2 in synergy across a wide range of scales to lead to their occurrence. The large and synoptic
3 scale conditions provided a favorable background (Figs. 1-3), and the development of the two
4 MCSs are undoubtedly tied closely to the forcings of the approaching front as well as the
5 terrain-influenced low-level convergence and moisture flux convergence associated with the
6 LLJ near northern Taiwan at meso- α and meso- β scales as described earlier. In Figs. 4 and 6,
7 the convective lines even exhibited characteristics of multiple lines at times, possibly linked
8 to gravity wave activities (e.g., Yang and Houze, 1995; Fovell et al., 2006). Given all these
9 driving mechanisms and forcings (at meso- β scale or larger), the BB process at convective
10 (meso- γ) scale was also a contributing factor leading to the extreme rainfall, especially during
11 the later 6 h period after 18:00 UTC. Also, as typical in many events, the new BB cell is often
12 found to develop about 15-30 km upstream from an old cell in Fig. 6. Thus, why this
13 particular spot has an advantage over other locations for new cell initiation within a common
14 background, rather than the mechanism for quasi-linear MCS development (such as frontal
15 and/or topographic forcings), is the scientific question that we wish to answer in this case
16 study. This specific question will be addressed through our numerical simulation results
17 below.

18

19 **4 Results of model simulation**

20 **4.1 Model result validation**

21 As described in Sect. 2.2, our CReSS model simulation was performed from 12:00 UTC 10
22 June 2012 for 48 h using NCEP (0.5°) final analyses as IC/BCs, with a horizontal grid spacing
23 of 1.5 km. The simulated winds and the front at an elevation of 549 m (close to 950 hPa) at
24 12:00 UTC 11 June ($t = 24$ h) and frontal positions every 6 h are shown in Fig. 2b and d.
25 Compared to the observation and NCEP analyses (Figs. 1, 2a, and 2e), the simulated front in
26 Fig. 2b is slightly too north, especially west of 120.5°E and over land in southeastern China,
27 but the prefrontal LLJ is well captured, including the strong winds near northern Taiwan.
28 Linked to the position error of the front at 12:00 UTC, the modeled front is also too north at
29 18:00 UTC, but its western segment over the strait advanced southward more rapidly to catch
30 up with the NCEP analyses during the next 6 h (Fig. 2c and d). The segment east of Taiwan,

1 however, is still too north at 00:00 UTC 12 June (cf. Fig. 2f) and the position error there does
2 not improve until about 12 h later (Fig. 2c and d).

3 The model-simulated surface winds at 10 m height and column-maximum mixing ratio of
4 total precipitation every 2 h during 12:00-22:00 UTC 11 June are shown in Fig. 7, which can
5 be compared with the radar composites in Fig. 4. In the model, the squall line before 18:00
6 UTC is along and to the north of the near-surface front (Fig. 7a-d) and different from the
7 training-line system ahead of the front in the observation. Thus, the simulation of the first
8 MCS was not ideal in location, apparently linked to the frontal position error discussed earlier.
9 On the other hand, the quasi-stationary MCS over northern Taiwan since 18:00 UTC, with
10 intense convective cells near Taipei, as well as the second squall line over the southern strait,
11 are both nicely captured in the model as the front advanced south (Fig. 7d-f). As a result, the
12 rainfall simulation in northern Taiwan during 18:00-24:00 UTC, with a peak amount of 312
13 mm, is in close agreement with the observation (Fig. 5b and d), while that during the
14 preceding 6 h was not (Fig. 5a and c). Similar results are also revealed by hourly histogram of
15 rainfall in Fig. 8, averaged inside the elongated box depicted in Fig. 5b. The rainfall in
16 northern Taiwan was much better simulated in magnitude and variation in time after 18:00
17 UTC 11 June (Fig. 8), although the areal-averaged intensity in the model is somewhat lower
18 because the simulated rain belt is narrower than the one observed (Fig. 5b and d). Also, the
19 model predicted more rainfall than observed over the mountains in southern Taiwan than (Fig.
20 5), indicating that the flow over the terrain might be somewhat over-estimated, though this is
21 not our focus here.

22 Figure 9 shows the development and evolution of convective cells over northern Taiwan and
23 the upstream area in the model every 10 min during 19:20-22:10 UTC. In this quasi-stationary
24 system (cf. Fig. 7d-f), the BB process is successfully simulated by CReSS. For example, a
25 new cell labeled as “A2” develops about 20 km upstream from the old cell “A1” around 19:30
26 UTC, and becomes mature near 20:10 UTC. Likewise, “B2” is triggered west of “B1” after
27 21:20 UTC, and develops into a mature cell near 21:40 UTC and then the two cells merge
28 near 21:50 UTC over northern Taiwan (Fig. 9), in a way similar to that discussed by WKJ15.
29 In the model, the training of multiple cells in succession clearly leads to heavy rainfall over
30 the Taipei area (cf. Fig. 7e and f), in agreement with the observation. Therefore, even though
31 the simulation of the first TL/AS MCS is less than ideal, the model results for the quasi-
32 stationary BB lines (after about 18:00 UTC 11 June) can be used to further investigate the BB

1 process upstream from the old cells in this case. Thus, the area and time period selected for
2 the separation of p_0 and p' , as described at the end of Sect. 2.3, are set to 24.75-25.15°N,
3 120.35-121.75°E (cf. Fig. 7a) and over 18:00-24:00 UTC 11 June 2012.

4 **4.2 Structure of convective cells in the BB MCS**

5 In this subsection, the simulated structure of convective cells inside the BB system is first
6 examined, before the discussion on the finer details of pressure perturbations and their
7 associated effects in the BB process. The pair of old and new cells for study has been chosen
8 to be B1 and B2 over the period of 20:00-21:40 UTC, as they are farther away and less
9 affected by the terrain of northern Taiwan (cf. Fig. 9). To reveal the storm environment
10 (provided by the forcings beyond storm scale), E-W vertical cross-sections along 25°N
11 through the centers of both B1 and B2 (line AB in Fig. 9) are constructed and averaged over
12 three outputs from 21:25 to 21:35 UTC, as shown in Fig. 10a. The equivalent potential
13 temperature (θ_e) has a minimum of about 350 K at mid-levels (near 4-5 km) and increases
14 both upward and downward in upstream as well as downstream regions, indicating the
15 presence of convective (and conditional) instability (cf. Fig 3). During the average period, the
16 mean updraft of B1 is located near 121.35°E (cf. Fig. 9), and its immediate upstream region,
17 i.e., where cell B2 is developing (~121.2°E), is characterized by strong near-surface
18 convergence coupled with upper-level divergence (Fig. 10a). Such a thermodynamic and
19 kinematic structure under the forcings of the front and terrain, clearly favorable for new cell
20 development upstream, is very similar to the composites of BB MCSs in the USA obtained by
21 Schumacher and Johnson (2005, their Fig. 17b). The WSW-ENE cross-section through B1
22 about 30 min earlier at 21:00 UTC shows a gradual acceleration of the upstream LLJ (thick
23 arrow line) under the forcing of background convergence. As the jet approaches B1, which is
24 already in mature stage, there is a rapid local acceleration then intense deceleration across B1,
25 by about 10 m s^{-1} with a convergence in excess of $5 \times 10^{-3} \text{ s}^{-1}$ (Fig. 10b). While this local
26 acceleration is clearly a response to the development of B1, the resulting vertical wind shear
27 from the south-southwest is strongest below 500 m under B1 and its immediate upstream,
28 where a value of about $2-3 \times 10^{-2} \text{ s}^{-1}$ can be reached (Fig. 10c). The vertical wind shear
29 upstream from B1 further aloft turns into northerly and then northeasterly at about 2 km, as
30 expected above the axis of the LLJ, but its value ($\sim 3 \times 10^{-3} \text{ s}^{-1}$) is one order of magnitude
31 smaller (Fig. 10c). Thus, the vertical wind shear in the storm environment of B1 (and B2) is

1 **strongest** near the surface. Also, the deep convection can be seen to tilt eastward with height
2 in both cross-sections, consistent with the direction of the upper-level winds and the evolution
3 of stratiform area (cf. Figs. 3 and 4).

4 The results of $\nabla^2 p'$ obtained by the two different methods (by separation and from Eqs. 3 and
5 4) as described in Sect. 2.3 at two different heights near 0.8 and 3 km are compared in Fig. 11,
6 also for 21:00 UTC as an example. In general, the patterns are very similar. At 0.8 km,
7 negative $\nabla^2 p'$ (implying $p' > 0$) occurs near the updraft of B1 with positive $\nabla^2 p'$ (implying p'
8 < 0) to the east near the downdraft (Fig. 11a and b). West of B1 where B2 is developing,
9 positive (negative) $\nabla^2 p'$ is found to the south (north) of the near-surface convergence zone.
10 Near 3 km, the updraft of B1 corresponds to $\nabla^2 p' > 0$ and $\nabla^2 p' < 0$ occurs to its western flank
11 and further upstream over B2 (Fig. 11d and e). The laplacian of buoyancy pressure
12 perturbation ($\nabla^2 p'_b$) alone computed from Eq. (3) closely resembles that of the total pressure
13 perturbations at both levels (except perhaps a slight southward shift near the updraft of B1 at
14 0.8 km), implying a dominant role of p'_b over p'_d in this event. Nevertheless, Fig. 11 confirms
15 that the two methods yield consistent results.

16 **4.3 Analysis of pressure perturbations**

17 To examine the distributions of pressure perturbations and their roles in the BB process in
18 greater details, a series of vertical cross-sections through the updraft center of B1 at 5 km and
19 the near-surface center of B2 from 20:00 to 21:00 UTC (each roughly 50 km in length, cf. Fig.
20 9), i.e., during the initiation stage of B2, are constructed. Here, the structures of $\nabla^2 p'$ are first
21 presented, so as to better infer to the patterns of p' discussed later through Eqs. (3) and (4). At
22 20:00 UTC when signs of B2 are yet to appear (Fig. 12a), the updraft of B1 ($>5 \text{ m s}^{-1}$) is more
23 upright with downdrafts at both flanks ($>1 \text{ m s}^{-1}$ at mid-level or above). At the backside
24 (upstream) of the updraft, in particular, $\nabla^2 p'$ is positive at mid-level and negative both above
25 and below, corresponding to $p' < 0$ and $p' > 0$, respectively (as labeled by “L” and “H”).
26 Again, the pattern of $\nabla^2 p'$ is largely attributable to its buoyant ($\nabla^2 p'_b$) instead of dynamical
27 component ($\nabla^2 p'_d$, Fig. 12b and c). Twenty minutes later at 20:20 UTC (Fig. 12d), the updraft
28 of B1 strengthens to more than 8 m s^{-1} and becomes more tilted, but the basic pattern of $\nabla^2 p'$
29 at its western flank and the upstream region remains. At this time, the suppressing downdraft
30 there weakens, and B2 is developing ($\sim 0.5 \text{ m s}^{-1}$) just west of the sinking motion and about
31 15 km upstream from the core of B1. This new development is associated with $p' < 0$ below 1

1 km and $p' > 0$ over 1-3 km, and the perturbations (and those of B1) are also mainly from the buoyant rather than dynamical effects (Fig. 12e and f).

3 At 20:40 UTC (Fig. 12g), B1 further strengthens and is even more tilted with height, and its associated downdraft below the mid-level ($> 2 \text{ m s}^{-1}$ near 4 km) now appears only at the eastern (downwind) side. The upward motion of B2 can now reach over 1 m s^{-1} and extends further upstream, while a layer of positive $\nabla^2 p'$ (implying $p' < 0$) forms near 5 km, again mainly from the buoyant effects (cf. Fig. 12h). The distribution of $\nabla^2 p'_d$ is only significant at both flanks of the updraft of B1 below about 3.5 km (and at its eastern flank near 5 km, Fig. 12i), which forms gradually as B1 intensifies (Fig. 12c and f). The configuration of positive (negative) p'_d at the rear (forward) flank of the updraft near 500 mm (below the jet level, cf. Fig. 10c) and a reversed pattern above (near 2-3 km) is consistent with the shearing (plus extension) effect (cf. Eq. 4), in agreement with WKJ15 and other earlier studies. However, since w and its horizontal gradient are weak near the surface, where the vertical wind shear is larger (also Fig. 10c), the value of $\nabla^2 p'_d$ is smaller than that in WKJ15. Also, due to the farther distance, a direct role played by the dynamical pressure perturbations in new cell initiation of B2 appears limited in the present case here.

17 Both B1 and B2 intensify at 21:00 UTC, and the latter, peaking at about 1.5 m s^{-1} , can now reach 4 km while the layer of $\nabla^2 p' > 0$ above (near 5 km) also grows stronger (Fig. 12j). A downdraft at the rear flank of B1 reappears at mid-levels and penetrates down to 3 km at this time, and acts to separate B2 from B1 (also Fig. 11d). Like earlier times since 20:20 UTC, the total pattern of $\nabla^2 p$ is dominated by $\nabla^2 p'_b$ everywhere, except near the based of B1 (below 1.5 km) where $\nabla^2 p'_d$ contributes significantly (Fig. 12k and l). Thus, the buoyancy-related effect is consistently the more dominant one in the region of B2 during its initiation stage in the model, suggesting the importance of moisture flux convergence in driving the development of the line-shaped MCS in this event (as discussed earlier in Sect. 3).

26 Nevertheless, the propagation speed of B1 is indeed slower than B2 in Fig. 9, and can be estimated to be about 8.9 m s^{-1} near 21:00 UTC. Caused by the dynamical effect of p'_d , this implies an increase in low-level convergence upstream by about $1 \times 10^{-4} \text{ s}^{-1}$ using Fig. 10b (with a LLJ of 12.5 m s^{-1} near 40 km upstream), or $2.2 \times 10^{-4} \text{ s}^{-1}$ larger than its surrounding with a background speed divergence of $\sim 1.2 \times 10^{-4} \text{ s}^{-1}$ following WKJ15. Since this is no

1 more than 20% of the maximum convergence near B2 and its immediate upstream (west of
2 121.2°E, cf. Fig. 10a), the minor role of p'_d in the present case can be confirmed.

3 The buoyancy B (or more precisely, the vertical buoyant force per unit mass) in Eq. (1) and its
4 contributing terms as given in Eq. (2) on the same vertical cross-sections are shown in Fig. 13.
5 At 20:00 UTC, as expected, B is positive inside the cumulonimbus B1, and negative in the top
6 portion of the cloud (> 6.5 km) and below the main updraft (< 2 km, Fig. 13a). Such a pattern
7 is due to the combined effects of positive virtual potential temperature perturbation ($\theta'_v > 0$)
8 clearly from latent heat release (LHR) inside the cloud, and the downward drag by all
9 hydrometeors (including both cloud particles and precipitation) maximized below the updraft
10 core (Fig. 13b and c). In the downdrafts at the flanks, B and $g(\theta'_v/\theta_{v0})$ are also mostly positive
11 from adiabatic warming outside the cloud.

12 From 20:20 to 21:00 UTC when the updraft of B1 becomes increasingly tilted, the buoyancy
13 B in the core region of the updraft remains positive because of LHR, as the drag force shifts
14 toward the downwind side (Fig. 13d-l). Below and east of the updraft, B is strongly negative
15 near the surface due to the drag and a rapid reduction in positive θ'_v as the air descends. Even
16 though this reduction in θ'_v suggests some evaporative cooling, the cold pool (and surface
17 outflow) would be to the east of B1. On the upstream side where B2 is developing, $B > 0$
18 appears near the surface with $B < 0$ further aloft at 2-5 km (Fig. 13d, g, and j) and can be
19 attributed, respectively, to LHR and adiabatic cooling associated with ascending motion (Fig.
20 13e, h, and k) in a convectively unstable environment. Apparently, as B2 develops, the
21 cooling above it and to the west (roughly 120.8-121°E) leads to a layer of positive $\partial B/\partial z$ and
22 $\nabla^2 p'_b$ near 5 km (cf. Eq. 3), since the air further above is stable (cf. Fig. 10a). In Fig. 13,
23 however, one particular center of negative B , near 120.85°E and 3 km at 20:20 UTC, develops
24 in a sinking area at the western edge of the cumulus, and therefore is also enhanced by
25 evaporative cooling of cloud droplets (Fig. 13d-l). Thus, the cooling and subsequently $B < 0$
26 (near 3 km) associated with B2 is not only by the adiabatic effect, but also by evaporation at
27 an earlier stage of initiation, for example, around 20:20 UTC (Fig. 13d and e). However, at
28 later times when the updraft of B1 becomes more tilted and B2 grows higher and stronger, it
29 becomes more difficult for the rear-flank downdraft to reach close to the surface (cf. Fig. 13j-
30 l), even though its strength can be sensitive to the cloud microphysical scheme (e.g., Morrison
31 et al., 2009).

1 Upstream from B1, the near-surface warming and cooling above, with maxima near 1 km and
2 3-4 km, respectively, create a decrease in buoyancy with height ($\partial B/\partial z < 0$) that grows
3 stronger with time near B2 (Fig. 13d, g, and j). Together with the (near) exponential decrease
4 of ρ_0 upward, this condition leads to $\nabla^2 p'_b < 0$ in Eq. (3), and thus $p'_b > 0$ that peaks slightly
5 above 1 km and intensifies through time, as obtained using the relaxation method (Sect. 2.3)
6 and shown in Fig. 14 (middle column). The upward decrease of p'_b , as the major component
7 of total p' , in turn produces an upward-directed buoyant PGF to help B2 develop further (Figs.
8 14, left and middle columns). Thus, the combined effect of buoyancy B (cf. Fig. 13, left
9 column) and total perturbation PGF in the vertical [cf. Eq. (1)] is upward acceleration of
10 parcels in B2 (Fig. 14, right column) to eventually reach free ascent and ignite deep
11 convection (near 21:20 UTC, cf. Fig. 9).

12

13 5 Discussion

14 In the previous section, the pressure perturbation and buoyancy, dominated by the
15 thermodynamic effects (including both adiabatic and diabatic ones from condensation or
16 evaporation), as well as the resultant upward development at the initiation stage of cell B2 are
17 examined (Figs. 11-14). The specific roles played by the old cell B1 in triggering B2,
18 however, are still not fully clear. Therefore, we further compare the initiation of an isolated
19 cell farther upstream, C1, where no existing cell is present nearby (cf. Fig. 9), with B1-B2
20 pair and discuss their differences. Obviously, cells like C1 can also develop on its own under
21 the background forcing, as also see in Fig. 6, but a comparison allows us to identify the
22 additional role of B1 to new cell triggering, and thus to the BB process about 15-30 km
23 upstream of the old cell in the present case.

24 Figure 15 shows similar plots as in Fig. 12, but through cell C1 on cross sections along the
25 low-level convergence zone (WSW-ENE oriented) at 20:40 and 21:20 UTC, at the beginning
26 of the initiation and right before the break out of deep convection, respectively (cf. Fig. 9). At
27 20:40 UTC (Fig. 15a), C1 is located near the left edge of the plots, while B2 appears near the
28 right edge. At this early stage, the weak rising motion is associated with $\nabla^2 p' > 0$ (or $p' < 0$)
29 below about 1 km and $\nabla^2 p' < 0$ (or $p' > 0$) slightly above near 1-2.5 km, again mostly from
30 the buoyant component (Fig. 15a-c). This pattern is because B is maximized near 1 km even
31 though its value is negative ($B < 0$) everywhere (not shown), indicating that the near-surface
32 atmosphere is still stable and the positive w is forced by the convergence at this time.

1 At 21:20 UTC when C1 grows much stronger ($\sim 1.5 \text{ m s}^{-1}$), the same pattern continues to
2 amplify and extends upward, while p'_d remains to play little role without a mature cell (Fig.
3 15d-f). Now, with clouds reaching about 5 km, B has become positive at the core of C1
4 (peaking over $2 \times 10^{-3} \text{ m s}^{-2}$ near 1.5 km) due to LHR after saturation (Fig. 16a and b), giving
5 a largest θ'_v of $\sim 1.2 \text{ K}$ (not shown). Near the cloud top and below the cloud base of C1, both
6 B and θ'_v turn negative and can only come from adiabatic or evaporative cooling, or both. The
7 cooling near 5-6 km explains the layer of $\nabla^2 p'_b$ (and $\nabla^2 p'$) > 0 immediately above (over 6-7
8 km, Fig. 15d and e), as seen earlier in Fig. 12g and 12j above the developing B2 (near 5 km).
9 The solutions of p' and p'_b by the relaxation method, linked to the pattern of their laplacian
10 noted above, produce downward perturbation PGF (below $\sim 2 \text{ km}$, Fig. 16c and d) that
11 partially cancel the upward buoyant force (cf. Fig. 16a).

12 Overall, the warming by LHR and the cooling above during the developing stage of new cells
13 represent a destabilization in their low-level environment with time (Figs. 13 and 16). Forced
14 by the background convergence, even though C1 eventually also develops into deep
15 convection, the vertical perturbation PGF remains pointing down below about 2.5 km even at
16 21:20 UTC (Fig. 16c and d). On the contrary, it is positive above 1-1.5 km in B2 and helps its
17 development at both 20:40 and 21:00 UTC (Fig. 14d and g). Consistent with this difference,
18 in B2, the maximum center of p'_b occurs closer to the surface and it decreases with height
19 more rapidly above, and three factors linked to the old cell B1 contribute to the establishment
20 of the upward-directed perturbation PGF. First, a stronger cooling occurs near 3 km above B2
21 (Fig. 13), at levels significantly lower than that above C1 (cf. Fig. 16), and this cooling is
22 enhanced by evaporation of condensates near the western edge of B1 (besides adiabatic
23 effect). Second, a more rapid and efficient warming also occurs closer to the surface at the
24 early stage of B2, and this is helped by the stronger LHR near the bottom of B1 (cf. Fig. 13).
25 Both these effects can be thought of as a more rapid destabilization that gives the new cell the
26 potential for a faster development. Finally, the separation by the descending branch of the old
27 cell, when such a descent can reach a lower elevation, also plays a role in leading to BB
28 process about 20 km upstream in the present case, based on our numerical simulation results
29 in this case study. In C1 where $B > 0$ is counteracted by a downward perturbation PGF, all
30 three advantages are absent without a nearby old cell (Figs. 15 and 16).

31

1 6 Conclusion and summary

2 During 11-12 June 2012 in the mei-yu season, both TL/AS and BB MCSs developed in
3 succession near northern Taiwan, and together produced extreme rainfall up to 510 mm
4 overnight in the Taipei metropolitan area, causing serious flooding in many densely-populated
5 regions. Observations show that BB behavior occurred in these MCSs, especially in the
6 second, E-W-aligned quasi-stationary linear MCS during 18:00-24:00 UTC 11 June (02:00-
7 08:00 LST 12 June), and was a contributing factor to the extreme rainfall and related hazards
8 in Taipei. The numerical simulation using the CReSS model with a horizontal grid size of 1.5
9 km starting at 12:00 UTC 10 June successfully captured the development and evolution of the
10 BB MCS (but with considerable position error for the preceding TL/AS system). Then, the
11 model results are used to investigate the details of the BB process occurring specifically about
12 15-30 km upstream from old convective elements in this subtropical system, where the cold
13 pool mechanism is not responsible for triggering new cells.

14 Although the dynamic pressure perturbations (p'_d) from the interaction between the mature
15 cells and the LLJ, with $p'_d > 0$ (< 0) at the rear (forward) flank of the updraft near the surface
16 below the jet and a reversed pattern near 2-3 km above the jet, can cause the mature cells to
17 slow-down slightly and enhance the low-level convergence upstream, their effects are weaker
18 compared to those found in WKJ15 for a case of typhoon rainband, and a direct role in new
19 cell initiation appears quite limited.

20 In the present event, the total pressure perturbations (p') in the vicinity of the new cell
21 throughout the initiation stage are attributed more to their buoyant (p'_b) than dynamical
22 component. Forced by the low-level convergence (parallel to the line) from the front and
23 induced by Taiwan terrain beyond storm scale in a convectively unstable storm environment,
24 the early development of new cells, at convective scale, are associated with positive buoyancy
25 ($B > 0$) by latent heating below and negative buoyancy ($B < 0$) by adiabatic cooling above,
26 and this represents a gradual destabilization in their surrounding environment. By comparing
27 the BB process with the initiation of an isolated cell, the additional and specific roles played
28 by the old cell to trigger new convection to its west can be identified. At the initial stage, the
29 development is close to the mature cell, which provides stronger warming below (and closer
30 to the surface) and also additional cooling above from evaporation of condensates at its rear
31 side. The more rapid upward decrease in B produces a positive p'_b at a lower height and
32 subsequently an upward-directed perturbation (buoyant) PGF that drives further development

1 together with the positive buoyancy. Thus, the net effect of the additional warming/cooling is
2 essentially a more rapid destabilization that gives the new cell a faster development. After
3 some time when the new cell has gain sufficient strength, a descending branch appearing at
4 the rear flank of the old cell acts to separate the new cell to about 20 km upstream. The new
5 cell continues to strengthen there, and eventually deep convection is ignited. Thus, the above
6 roles played by the existing old cells, largely thermodynamic in origin but also helped by
7 dynamical and kinematic effects, can explain why the spot roughly 15-30 km upstream from
8 the western end of quasi-linear MCSs in the subtropics **can often have** advantages over other
9 locations for new cell initiation in their back-building process, even in the absence of cold
10 pool mechanism.

11

12 **Acknowledgements**

13 The authors wish to acknowledge the CWB and NCEP in providing the various data used in
14 this study, and the helps from Mr. C.-Y. Lee in programming, and Mr. K.-Y. Chen and Ms.
15 S.-Y. Huang in making some of the figures. This study is jointly supported by the Ministry of
16 Science and Technology of Taiwan under Grants MOST-103-2119-M-003-001-MY2 and
17 MOST-103-2625-M-003-001-MY2.

18

19 **Appendix The relaxation method**

20 In this study, the relaxation method is used to numerically solve for the pressure perturbation
21 p from its 3-D laplacian $\nabla^2 p$ (“prime” omitted for simplicity), where $\nabla^2 p$ can be $\nabla^2 p_b$, $\nabla^2 p_d$,
22 or any of the rhs terms in Eq. (3) or (4). In this appendix, its formulation and boundary
23 conditions are described. Since the vertical grid spacing of CReSS is stretched, the values of
24 $\nabla^2 p$ (and all other known variables in need) are first vertically interpolated to grid with a fixed
25 Δz of 100 m, such that $\Delta x = \Delta y = 1 \text{ km} = 10 \Delta z$. At second-order accuracy, the 3-D laplacian
26 inside the calculation domain is approximated by the central-difference method as

$$27 \quad \nabla^2 p = \frac{p_{x+1} + p_{x-1} - 2p}{\Delta x^2} + \frac{p_{y+1} + p_{y-1} - 2p}{\Delta y^2} + \frac{p_{z+1} + p_{z-1} - 2p}{\Delta z^2} \quad (\text{A1})$$

1 where subscripts represent the p values of the next grid point on either side in each direction.
 2 After rearranging terms to move only p (unknown) on the lhs and using $\Delta x = \Delta y = 10 \Delta z$, Eq.
 3 (A1) can be rewritten as

$$4 \quad p = \frac{p_{x+1} + p_{x-1} + p_{y+1} + p_{y-1} + 10^2(p_{z+1} + p_{z-1}) - (\Delta x^2 \cdot \nabla^2 p)}{4 + 2 \times 10^2} \quad (\text{A2})$$

5 and used for interior grid points. On the boundary of the domain, the Neumann condition is
 6 applied and the next grid point outside is assumed to have the same value as the one on the
 7 boundary. For example, $p_{x-1} = p$ on the western boundary, and the laplacian in x -direction
 8 ($\nabla^2 p_x$) in (A1) reduces to

$$9 \quad \nabla^2 p_x = \frac{p_{x+1} - p}{\Delta x^2} \quad (\text{A3})$$

10 while the two other rhs terms in y and z directions remain unchanged. So, on the western
 11 boundary, the p_{x-1} term vanishes and the formula equivalent to Eq. (A2) becomes

$$12 \quad p = \frac{p_{x+1} + p_{y+1} + p_{y-1} + 10^2(p_{z+1} + p_{z-1}) - (\Delta x^2 \cdot \nabla^2 p)}{3 + 2 \times 10^2}. \quad (\text{A4})$$

13 Thus, on each of the remaining sides (and edges and corners) along the boundary of the 3-D
 14 domain, the formula would take a different form from (A2) following a similar derivation.
 15 Since the procedures are quite straight-forward, they are not repeated here.

16 Using equations including (A2) and (A4), the values of p can be numerically solved through
 17 iteration. Starting from a set of first guess of p , all the terms on the RHS are known or can be
 18 computed, and a new set of p on the LHS is obtained in each iteration going through all the
 19 grid points. After each iteration, Eq. (A1) (or its equivalents on the boundaries) is used to
 20 compute $\nabla^2 p$ from the newly-obtained p and check against the true value (from Eqs. 3 or 4).
 21 When the total absolute error of $\nabla^2 p$ summed over all grid points reduces below the specified
 22 threshold, the result converges and the iteration stops. Figures 13 and 15 of WKJ15 provide
 23 some examples of the results obtained using the same relaxation method.

24

1 **References**

- 2 Bluestein, H. B., and Jain, M. H.: Formation of mesoscale lines of precipitation: severe squall
3 lines in Oklahoma during the spring, *J. Atmos. Sci.*, 42, 1711-1732, 1985.
- 4 Brooks, H. E., and Stensrud, D. J.: Climatology of heavy rain events in the United States from
5 hourly precipitation observations, *Mon. Weather Rev.*, 128, 1194-1201, 2000.
- 6 Browning, K. A.: Organization of clouds and precipitation in extratropical cyclones, in:
7 *Extratropical Cyclones: The Erik Palmén Memorial Volume*, edited by: Newton, C. W. and
8 Holopainen, E. O., Am. Meteor. Soc., Boston, MA, USA, 129-153, 1990.
- 9 Carbone, R. E.: A severe frontal rainband. Part I: Stormwide hydrodynamic structure, *J.*
10 *Atmos. Sci.*, 39, 258-279, 1982.
- 11 Chappell, C. F.: Quasi-stationary convective events, in: *Mesoscale Meteorology and*
12 *Forecasting*, edited by: Ray, P., Am. Meteor. Soc., Boston, MA, USA, 289-310, 1986.
- 13 Chen, G. T.-J., and Chou, H.-C.: General characteristics of squall lines observed in TAMEX,
14 *Mon. Weather Rev.*, 121, 726-733, 1993.
- 15 Chen, G. T.-J., Wang, C.-C., and Lin, D. T.-W.: Characteristics of low-level jets over
16 northern Taiwan in Mei-yu season and their relationship to heavy rain events, *Mon.*
17 *Weather Rev.*, 133, 20-43, 2005.
- 18 Corfidi, S. F.: Cold pools and MCS propagation: **forecasting** the motion of downwind-
19 developing MCSs, *Weather Forecast.*, 18, 997-1017, 2003.
- 20 Corfidi, S. F., Meritt, J. H., and Fritsch, J. M.: Predicting the movement of mesoscale
21 convective complexes, *Weather Forecast.*, 11, 41-46, 1996.
- 22 Cotton, W. R., Tripoli, G. J., Rauber, R. M., and Mulvihill, E. A.: Numerical simulation of the
23 effects of varying ice crystal nucleation rates and aggregation processes on orographic
24 snowfall, *J. Clim. Appl. Meteorol.*, 25, 1658-1680, 1986.
- 25 Doswell, C. A., III: Severe convective storms – an overview, in: *Severe Convective Storms*,
26 *Meteor. Monogr.*, No. 50, Am. Meteor. Soc., Boston, MA, USA, ISBN: 978-1-878220-41-
27 7, 1-26, 2001.
- 28 Doswell, C. A., III, Brooks, H. E., and Maddox, R. A.: Flash flood forecasting: **an**
29 ingredients-based methodology, *Weather Forecast.*, 11, 560-581, 1996.

- 1 Fovell, R. G., Mullendore, G. L., and Kim, S.-H.: Discrete propagation in numerically
2 simulated nocturnal squall lines, *Mon. Weather Rev.*, 134, 3735-3752, 2006.
- 3 Houston, A. L., and Wilhelmson, R. B.: Observational analysis of the 27 May 1997 central
4 Texas tornadic event. Part I: Prestorm environment and storm maintenance/propagation,
5 *Mon. Weather Rev.*, 135, 701-726, 2007.
- 6 Houze, R. A., Jr., Smull, B. F., and Dodge, P.: Mesoscale organization of springtime
7 rainstorms in Oklahoma, *Mon. Weather. Rev.*, 118, 613-654, 1990.
- 8 Hsu, J.: ARMTS up and running in Taiwan, *Väisälä News*, 146, 24-26, 1998.
- 9 Ikawa, M., and Saito, K.: Description of a nonhydrostatic model developed at the Forecast
10 Research Department of the MRI, MRI Tech. Rep. 28, Tsukuba, Japan, 238 pp, 1991.
- 11 James, R. P., and Markowski, P. M.: A numerical investigation of the effects of dry air aloft
12 on deep convection, *Mon. Weather Rev.*, 138, 140-161, 2010.
- 13 Jeong, J.-H., Lee, D.-I., and Wang, C.-C.: A study on an extreme rainfall-producing quasi-
14 stationary mesoscale convective system over southeastern Korea. Impact of cold pool,
15 *Mon. Weather Rev.*, revised, 2016.
- 16 Johnson, R. H., and Mapes, B. E.: Mesoscale processes and severe convective weather, in:
17 Severe Convective Storms, edited by: Doswell, C. A., III, Meteor. Monogr., No. 50, Am.
18 Meteor. Soc., Boston, MA, USA, ISBN: 978-1-878220-41-7, 71-122, 2001.
- 19 Jou, B. J.-D., and Deng, S.-M.: Structure of a low-level jet and its role in triggering and
20 organizing moist convection over Taiwan: A TAMEX case study. *Terr. Atmos. Oceanic
21 Sci.*, 3, 39-58, 1992.
- 22 Klemp, J. B.: Dynamics of tornadic thunderstorms, *Annu. Rev. Fluid Mech.*, 19, 369-402,
23 1987.
- 24 Kondo, J.: Heat balance of the China Sea during the air mass transformation experiment, *J.
25 Meteor. Soc. Jpn.*, 54, 382-398, 1976.
- 26 LeMone, M. A., Zipser, E. J., and Trier, S. B.: The role of environmental shear and
27 thermodynamic conditions in determining the structure and evolution of mesoscale
28 convective systems during TOGA COARE, *J. Atmos. Sci.*, 55, 3493-3518, 1998.
- 29 Li, J., and Chen, Y.-L.: Barrier jets during TAMEX, *Mon. Weather Rev.*, 126, 959-971, 1998.

- 1 Li, J., Chen, Y.-L., and Lee, W.-C.: Analysis of a heavy rainfall event during TAMEX, Mon.
2 Weather Rev., 125, 1060-1082, 1997.
- 3 Lin, Y.-L., Farley, R. D., and Orville, H. D.: Bulk parameterization of the snow field in a
4 cloud model, *J. Clim. Appl. Meteorol.*, 22, 1065-1092, 1983.
- 5 Louis, J. F., Tiedtke, M., and Geleyn, J. F.: A short history of the operational PBL –
6 parameterization at ECMWF, in: Proceedings, ECMWF Workshop on Planetary Boundary
7 Layer Parameterization, Reading, UK, 59-79, 1981.
- 8 Luo, Y., Gong, Y., and Zhang, D.-L.: Initiation and organizational modes of an extreme-rain-
9 producing mesoscale convective system along a Mei-yu front in East China, Mon. Weather
10 Rev., 142, 203-221, 2014.
- 11 Morrison, H., Thompson, G., and Tatarskii, V.: Impact of cloud microphysics on the
12 development of trailing stratiform precipitation in a simulated squall line: Comparison of
13 one- and two-moment schemes, *Mon. Weather Rev.*, 137, 991-1007, 2009.
- 14 Maddox, R. A., Chappell, C. F., and Hoxit, L. R.: Synoptic and meso- α scale aspects of flash
15 flood events, *Bull. Am. Meteor. Soc.*, 60, 115-123, 1979.
- 16 Meng, Z., Yan, D., and Zhang, Y.: General features of squall lines in East China, Mon.
17 Weather Rev., 141, 1629-1647, 2013.
- 18 Moore, B. J., Neiman, P. J., Ralph, F. M., and Barthold, F. E.: Physical processes associated
19 with heavy flooding rainfall in Nashville, Tennessee, and vicinity during 1-2 May 2010:
20 The role of an atmospheric river and mesoscale convective systems, *Mon. Weather Rev.*,
21 140, 358-378, 2012.
- 22 Murakami, M.: Numerical modeling of dynamical and microphysical evolution of an isolated
23 convective cloud---The 19 July 1981 CCOPE cloud, *J. Meteor. Soc. Jpn.*, 68, 107-128,
24 1990.
- 25 Murakami, M., Clark, T. L., and Hall, W. D.: Numerical simulations of convective snow
26 clouds over the Sea of Japan: two-dimensional simulation of mixed layer development and
27 convective snow cloud formation, *J. Meteor. Soc. Jpn.*, 72, 43-62, 1994.
- 28 Parker, M. D., and Johnson, R. H.: Organizational modes of midlatitude mesoscale convective
29 systems, *Mon. Weather Rev.*, 128, 3413-3436, 2000.

- 1 Parker, M. D., and Johnson, R. H.: Structures and dynamics of quasi-2D mesoscale
2 convective systems, *J. Atmos. Sci.*, 61, 545-567, 2004.
- 3 Peters, J. M., and Roebber, P. J.: Synoptic control of heavy-rain-producing convective
4 training episodes, *Mon. Weather Rev.*, 142, 2464-2482, 2014.
- 5 Peters, J. M., and Schumacher, R. S.: Mechanisms for organization and echo training in a
6 flash-flood-producing mesoscale convective system, *Mon. Weather Rev.*, 143, 1058-1085,
7 2015.
- 8 Rotunno, R., and Klemp, J. B.: The influence of the shear-induced pressure gradient on
9 thunderstorm motion, *Mon. Weather Rev.*, 110, 136-151, 1982.
- 10 Rotunno, R., Klemp, J. B., and Weisman, M. L.: A theory for strong, long-lived squall lines, *J.*
11 *Atmos. Sci.*, 45, 463-485, 1988.
- 12 Schumacher, R. S., and Johnson, R. H.: Organization and environmental properties of
13 extreme-rain-producing mesoscale convective systems, *Mon. Weather Rev.*, 133, 961-976,
14 2005.
- 15 Schumacher, R. S., and Johnson, R. H.: Characteristics of U.S. extreme rain events during
16 1999-2003, *Weather Forecast.*, 21, 69-85, 2006.
- 17 Schumacher, R. S., and Johnson, R. H.: Quasi-stationary, extreme-rain-producing convective
18 systems associated with midlevel cyclonic circulations, *Weather Forecast.*, 24, 555-574,
19 2009.
- 20 Segami, A., Kurihara, K., Nakamura, H., Ueno, M., Takano, I., and Tatsumi, Y.: Operational
21 mesoscale weather prediction with Japan Spectral Model, *J. Meteor. Soc. Jpn.*, 67, 907-924,
22 1989.
- 23 Stevenson, S. N., and Schumacher, R. S.: A 10-year survey of extreme rainfall events in the
24 central and eastern United States using gridded multisensor precipitation analyses, *Mon.*
25 *Weather Rev.*, 142, 3147-3162, 2014.
- 26 Sun, J., and Lee, T.-Y.: A numerical study of an intense quasi-stationary convection band
27 over the Korean Peninsula, *J. Meteor. Soc. Jpn.*, 80, 1221-1245, 2002.
- 28 Tompkins, A. M.: Organization of tropical convection in low vertical wind shears: The role of
29 cold pools, *J. Atmos. Sci.*, 58, 1650-1672, 2001.

- 1 Tsuboki, K., and Sakakibara, A.: Large-scale parallel computing of cloud resolving storm
2 simulator, in: High Performance Computing, edited by: Zima, H. P., Joe, K., Sato, M., Seo,
3 Y., and Shimasaki, M., Springer-Verlag, Berlin and Heidelberg, Germany; New York, NY,
4 USA, ISBN: 978-3-540-47847-8, 243-259, 2002.
- 5 Tsuboki, K., and Sakakibara, A.: Numerical Prediction of High-Impact Weather Systems: *the*
6 Textbook for the Seventeenth IHP Training Course in 2007, Hydrospheric Atmospheric
7 Research Center, Nagoya University and UNESCO, Nagoya, Japan, ISBN: 978-4-
8 9980619-8-4, 273 pp, 2007.
- 9 Wang, C.-C.: 2015: The more rain, the better the model performs---The dependency of
10 quantitative precipitation forecast skill on rainfall amount for typhoons in Taiwan, *Mon.*
11 *Weather Rev.*, 143, 1723-1748, 2015.
- 12 Wang, C.-C., and Huang, W.-M.: High-resolution simulation of a nocturnal narrow
13 convective line off the southeastern coast of Taiwan in the mei-yu season, *Geophys. Res.*
14 *Lett.*, 36, L06815, doi:10.1029/2008GL037147, 2009.
- 15 Wang, C.-C., Chen, G. T.-J., Chen, T.-C., and Tsuboki, K.: A numerical study on the effects
16 of Taiwan topography on a convective line during the mei-yu season, *Mon. Weather Rev.*,
17 133, 3217-3242, 2005.
- 18 Wang, C.-C., Chen, G. T.-J., and Huang, S.-Y.: Remote trigger of deep convection by cold
19 outflow over the Taiwan Strait in the Mei-yu season: A modeling study of the 8 June 2007
20 case, *Mon. Weather Rev.*, 139, 2854-2875, 2011.
- 21 Wang, C.-C., Kuo, H.-C., Chen, Y.-H., Huang, H.-L., Chung, C.-H., and Tsuboki, K.: Effects
22 of asymmetric latent heating on typhoon movement crossing Taiwan: The case of Morakot
23 (2009) with extreme rainfall, *J. Atmos. Sci.*, 69, 3172-3196, 2012.
- 24 Wang, C.-C., Kuo, H.-C., Yeh, T.-C., Chung, C.-H., Chen, Y.-H., Huang, S.-Y., Wang, Y.-W.,
25 and Liu, C.-H.: High-resolution quantitative precipitation forecasts and simulations by the
26 Cloud-Resolving Storm Simulator (CReSS) for Typhoon Morakot (2009), *J. Hydrol.*, 506,
27 26-41, <http://dx.doi.org/10.1016/j.jhydrol.2013.02.018>, 2013.
- 28 Wang, C.-C., Hsu, J. C.-S., Chen, G. T.-J., and Lee, D.-I.: A study of two propagating heavy-
29 rainfall episodes near Taiwan during SoWMEX/TiMREX IOP-8 in June 2008. Part I:
30 Synoptic evolution, episode propagation, and model control simulation, *Mon. Weather*
31 *Rev.*, 142, 2619-2643, 2014a.

- 1 Wang, C.-C., Hsu, J. C.-S., Chen, G. T.-J., and Lee, D.-I.: A study of two propagating heavy-
2 rainfall episodes near Taiwan during SoWMEX/TiMREX IOP-8 in June 2008. Part II:
3 Sensitivity tests on the roles of synoptic conditions and topographic effects, *Mon. Weather*
4 *Rev.*, 142, 2644-2664, 2014b.
- 5 Wang, C.-C., Kuo, H.-C., Johnson, R.-H., Lee, C.-Y., Huang, S.-Y., and Chen, Y.-H.: A
6 numerical study of convection in rainbands of Typhoon Morakot (2009) with extreme
7 rainfall: Roles of pressure perturbations with low-level wind maxima, *Atmos. Chem. Phys.*,
8 [15, 11097-11115, doi:10.5194/acp-15-11097-2015](https://doi.org/10.5194/acp-15-11097-2015), 2015.
- 9 Wang, C.-C., Huang, S.-Y., Chen, S.-H., Chang, C.-S., and Tsuboki, K.: Cloud-resolving
10 typhoon rainfall ensemble forecasts for Taiwan with large domain and extended range
11 through time-lagged approach, *Weather Forecast.*, 31, 151-172, 2016.
- 12 Wang, H., Luo, Y.-L., and Jou, B. J.-D.: Initiation, maintenance, and properties of convection
13 in an extreme rainfall event during SCMREX: **observational** analysis, *J. Geophys. Res.*
14 *Atmos.*, 119: 13206-13232, doi: 10.1002/2014JD022339, 2014.
- 15 Weisman, M. L., and Klemp, J. B.: Characteristics of isolated convective storms, in:
16 *Mesoscale Meteorology and Forecasting*, edited by: Ray, P. S., Am. Meteor. Soc., Boston,
17 MA, USA, 331-358, 1986.
- 18 Weisman, M. L., and Rotunno, R.: "A theory for strong long-lived squall lines" revisited, *J.*
19 *Atmos. Sci.*, 61, 361-382, 2004.
- 20 Wilhelmson, R. B., and Ogura, Y.: The pressure perturbation and the numerical modeling of a
21 cloud, *J. Atmos. Sci.*, 29, 1295-1307, 1972.
- 22 Xu, W., Zipser, E. J., Chen, Y.-L., Liu, C., Liou, Y.-C., Lee, W.-C., and Jou, B. J.-D.: An
23 orography-associated extreme rainfall event during TiMREX: Initiation, storm evolution,
24 and maintenance, *Mon. Weather Rev.*, 140, 2555-2574, 2012.
- 25 [Yang, M.-J., and Houze, R. A., Jr.: Multicell squall-line structure as a manifestation of](#)
26 [vertically trapped gravity waves. *Mon. Weather Rev.*, 123, 641-661, 1995.](#)
- 27 Yeh, H.-C., and Chen, Y.-L.: The role of offshore convergence on coastal rainfall during
28 TAMEX IOP 3, *Mon. Weather Rev.*, 130, 2709-2730, 2002.
- 29 Yu, C.-K., and Chen, Y.: Surface fluctuations associated with tropical cyclone rainbands
30 observed near Taiwan during 2000-08, *J. Atmos. Sci.*, 68, 1568-1585, 2011.

1 Zhang, M., and Zhang, D.-L.: Subkilometer simulation of a torrential-rain-producing
2 mesoscale convective system in East China. Part I: Model verification and convective
3 organization, *Mon. Weather Rev.*, 140, 184-201, 2012.

4

1 Table 1. The CReSS model domain configuration and physics used in this study.

2

Projection	Lambert Conformal (center at 120°E, secant at 10°N and 40°N)
Grid spacing	1.5 km × 1.5 km × 100-980 m (400 m)*
Dimension and size (<i>x, y, z</i>)	1000 × 800 × 50 (1500 km × 1200 km × 20 km)
IC/BCs	NCEP 0.5° × 0.5° analyses (26 levels, every 6 h)
Topography and SST	Real at (1/120)° and weekly mean on 1° × 1° grid
Integration period	1200 UTC 10 Jun to 1200 UTC 12 Jun 2012 (48 h)
Output frequency	Every 15 min (every 5 min during 1800-2400 UTC 11 Jun)
Cloud microphysics	Bulk cold-rain scheme (6 species)
PBL parameterization	1.5-order closure with prediction of turbulent kinetic energy
Surface processes	Energy/momentum fluxes, shortwave and longwave radiation
Substrate soil model	41 levels, every 5 cm to 2m deep

3 * The vertical grid spacing (Δz) of CReSS is stretched (smallest at the bottom), and the
4 averaged spacing is given in the parentheses.

5

1 **Figure captions**

2 Figure 1. CWB surface analyses and positions of front/trough (or wind-shift line, thick dashed)
3 at 850 (red), 700 (blue), 500 (green), and 200 hPa (orange) at 12:00 UTC 11 Jun 2012. The
4 CReSS model domain is marked by the dotted box.

5 Figure 2. (a) NCEP (0.5°) 950 hPa analysis and (b) CReSS simulation of horizontal winds (m
6 s^{-1} , speed shaded, scale to the right) at $z = 549$ m at 12:00 UTC 11 Jun 2012, with frontal
7 position marked (thick dashed lines). (c, d) Frontal positions every 6 h from 06:00 UTC 11
8 Jun to 12:00 UTC 12 Jun 2012 (c) at 950 hPa in NCEP analyses and (d) at $z = 549$ m in model
9 (see legend for line color and style), overlaid with topography (km, shading, scale to the right).
10 The triangle in (c) marks the location of Panchiao sounding in Fig. 3. (e, f) ASCAT oceanic
11 winds ($m s^{-1}$) near Taiwan at (e) 13:00 UTC 11 Jun and (f) 02:00 UTC 12 Jun, 2012, with
12 surface frontal position analyzed.

13 Figure 3. Thermodynamic (skew T -log p) diagram for the sounding taken at Panchiao (46692,
14 cf. Fig. 2c for location) at 12:00 UTC 11 Jun 2012. For winds, full (half) barbs denote 10 (5)
15 kts (1 kt = $0.5144 m s^{-1}$), respectively.

16 Figure 4. Composite VMI radar reflectivity (dBZ, color, scale to the right) over the Taiwan
17 area at 1 h intervals from (a) 12:00 UTC 11 Jun to (i) 02:00 UTC 12 Jun, 2012. The outline of
18 Taiwan is highlighted (thick dotted lines) and the surface frontal position is plotted at synoptic
19 times (thick dashed lines).

20 Figure 5. Distribution of observed 6-h accumulated rainfall (mm, color, scale to the right)
21 over Taiwan during (a) 12:00-18:00 UTC and (b) 18:00-24:00 UTC 11 Jun 2012. The Taipei
22 City boundary is depicted in panel (a), and the dotted box in (b) shows the region used in Fig.
23 8 for rainfall average. (c, d) As in (a, b), but showing model-simulated rainfall over Taiwan
24 and the surrounding oceans.

25 Figure 6. As in Fig. 4, but showing reflectivity over northern Taiwan and the upstream area
26 every 10 min from (a) 19:40 UTC to (o) 22:00 UTC 11 Jun 2012 using a different set of
27 colors. The arrows mark the initiation or strengthening of back-building cells, off the western
28 end of a rainband or upstream from an old cell.

29 Figure 7. CReSS simulation of surface winds at 10 m height ($m s^{-1}$) and column-maximum
30 mixing ratio of precipitation (rain + snow + graupel, $g kg^{-1}$, shading, scale to the right) every

1 2 h from (a) 12:00 UTC to (f) 22:00 UTC 11 Jun 2012. For winds, full (half) barbs denote 10
2 (5) m s^{-1} , and the surface frontal positions are marked (thick dashed lines). The rectangle in
3 panel (a) depicts the area (24.75-25.15°N, 120.35-121.75°E) used for the separation method.

4 Figure 8. Time series of observed (gray bars) and simulated (curve with dots) hourly rainfall
5 (mm), averaged inside the box shown in Fig. 5b (24.75-25.17°N, 120.87-121.85°E) over
6 northern Taiwan from 12:00 UTC 11 Jun to 06:00 UTC 12 Jun 2012.

7 Figure 9. Model-simulated column-maximum vertical velocity (w , m s^{-1} , color and thin
8 contours) every 10 min during 19:20-22:10 UTC 11 Jun 2012, overlaid with terrain elevation
9 (m, thick contours at 250 and 500 m) in northern Taiwan. The color scale is shown at the
10 bottom, and the contour at 0.5 m s^{-1} is not drawn. Old cells (A1, B1, and C1) and nearby new
11 cells (A2, B2) of interests are labeled. Green dashed lines AB and CD depict the vertical
12 cross-sections used in Fig. 10, and the short segments depict those used in Figs. 12-16 (blue
13 (brown) ones through B1 (C1)).

14 Figure 10. (a) E-W vertical cross-section of model-simulated convergence/divergence (10^{-4}
15 s^{-1} , color, positive for convergence) and θ_e (K, contour, every 1 K) along 25°N (line AB in
16 Fig. 9), averaged over 21:25-21:35 UTC 11 Jun 2012. The triangle marks the mean location
17 of the updraft of B1. (b, c) As in panel (a), except showing (b) convergence/divergence (color)
18 and wind vectors (m s^{-1}) and speed (isotach every 1 m s^{-1}) and (c) w (m s^{-1} , color) and
19 vertical wind shear vector (10^{-3} s^{-1} , in cordinal direction, reference vectors both plotted)
20 along the WSW-ENE section (line CD in Fig. 9) at 21:00 UTC 11 Jun 2012. Thick arrow-
21 lines in (b, c) depict the axis of the LLJ.

22 Figure 11. Model-simulated w (m s^{-1} , color, scale at bottom) and laplacian of perturbation
23 pressure ($10^{-6} \text{ Pa m}^{-2}$, contour, every $3 \times 10^{-6} \text{ Pa m}^{-2}$, dashed for negative values) of cells B1
24 and B2 at (left) 806 m and (right) 2929 m at 21:00 UTC 11 Jun 2012. (a, d) $\nabla^2 p'$ obtained
25 from separation method, and (b, e) $\nabla^2 p' = \nabla^2 p'_b + \nabla^2 p'_d$ and (c, f) $\nabla^2 p'_b$ computed from Eqs.
26 (3) and (4). Cells B1 and B2 and updraft and downdraft centers are labeled in panels (a) and
27 (d).

28 Figure 12. Vertical cross-sections of model-simulated w (m s^{-1} , color) and (a) $\nabla^2 p'$ (10^{-6} Pa
29 m^{-2}) and wind vectors (m s^{-1} , reference vector at bottom) on section plain, (b) $\nabla^2 p'_b$
30 (computed from Eq. 3), and (c) $\nabla^2 p'_d$ (computed from Eq. 4) and vertical wind shear vector

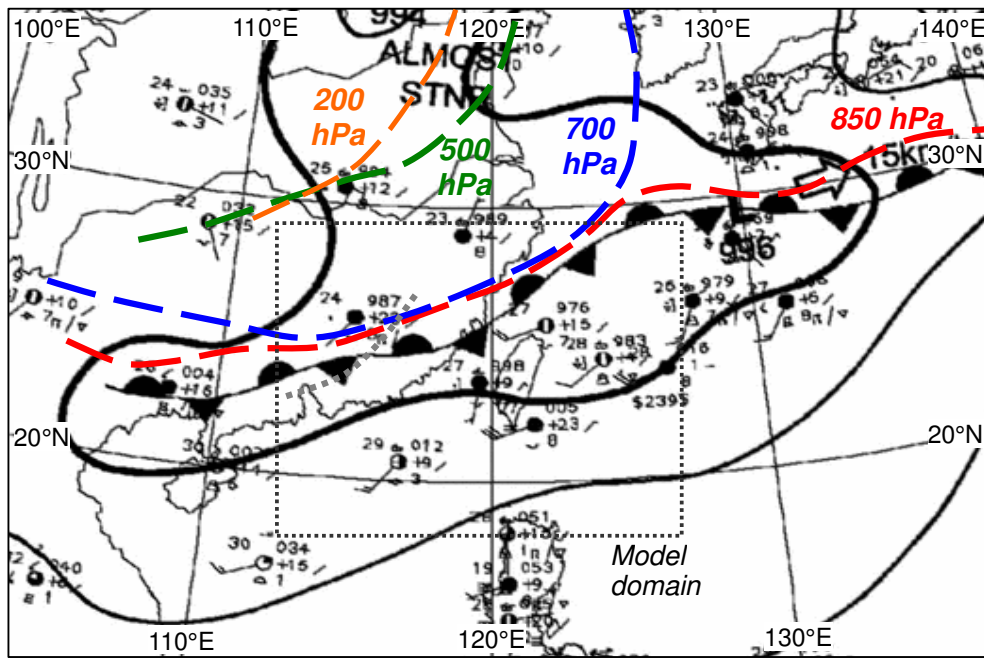
1 (10^{-3} s^{-1} , in cardinal direction, reference vector at bottom) along the E-W segment through B1
2 and B2 at 20:00 UTC 11 Jun 2012 (cf. Fig. 9). All contour intervals are $3 \times 10^{-6} \text{ Pa m}^{-2}$ (zero
3 line omitted, dashed for negative values), and letters H (L) denote corresponding high (low)
4 pressure perturbations. (d-f), (g-i), and (j-l) As in (a-c), except at 20:20, 20:40, 21:00 UTC
5 (WNW-ESE segments for 20:40 and 21:00 UTC, cf. Fig. 9), respectively.

6 Figure 13. (a-c) As in Fig. 12a-c, but showing w and (a) buoyancy B (10^{-3} m s^{-2} , black
7 contour) and mixing ratio of cloud particles (g kg^{-1} , blue contour, every 3 g kg^{-1}), (b)
8 $g(\theta'_v/\theta_{v0})(10^{-3} \text{ m s}^{-2})$, and (c) $-g \sum q_x$ (10^{-3} m s^{-2}). All black contour intervals are $3 \times 10^{-6} \text{ Pa}$
9 m^{-2} (dashed for negative values, zero line omitted), and + (–) signs denote upward
10 (downward) maxima. (d-f), (g-i), and (j-l) As in (a-c), except at 20:20, 20:40, and 21:00 UTC,
11 respectively.

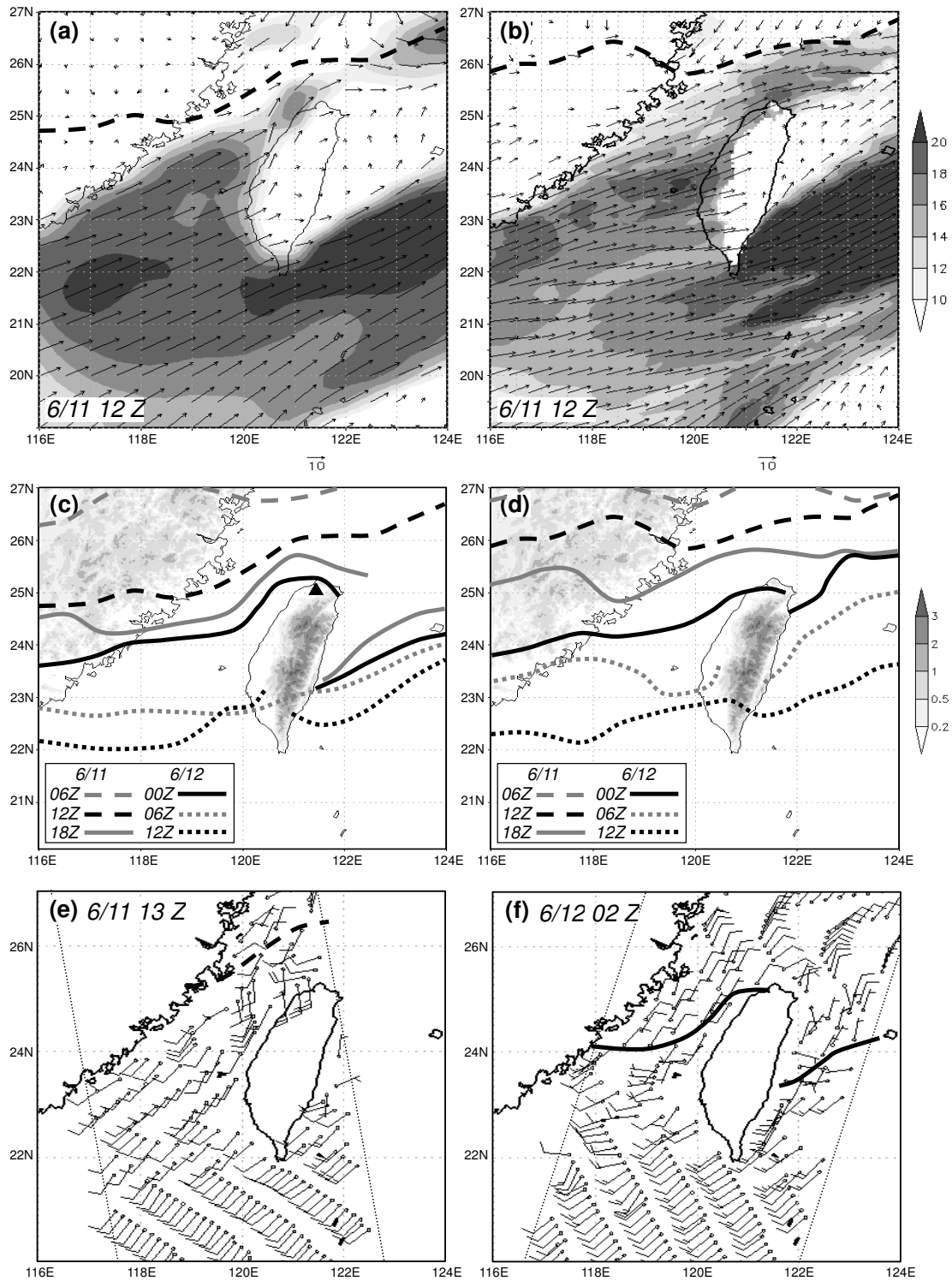
12 Figure 14. As in Fig. 13, but showing w and (a, d, g) $p' = p'_b + p'_d$ (Pa, black contour, every
13 10 Pa, dashed for negative values) obtained from the relaxation method and the corresponding
14 perturbation PGF in the vertical ($-(\partial p'/\partial z)/\rho_0$, 10^{-3} m s^{-2} , blue contour), (b, e, h) p'_b (Pa) and
15 its vertical PGF (10^{-3} m s^{-2}), and (c, f, i) dw/dt from vertical perturbation PGF and B (10^{-3} m
16 s^{-2} , black contour). For force (per unit mass) and acceleration, all contour intervals are $5 \times$
17 10^{-3} m s^{-2} (dashed for negative values), and upward (downward) arrows denote maxima
18 (minima).

19 Figure 15. As in Fig. 12, but showing w (m s^{-1} , color) and (a) $\nabla^2 p'$ ($10^{-6} \text{ Pa m}^{-2}$) and wind
20 vectors (m s^{-1}) on section plain, (b) $\nabla^2 p'_b$, and (c) $\nabla^2 p'_d$ and vertical wind shear vector (10^{-3}
21 s^{-1} , in cardinal direction) along the WSW-ENE segment through C1 at 20:40 UTC 11 Jun
22 2012 (cf. Fig. 9). (d-f) As in (a-c), except at 21:20 UTC.

23 Figure 16. (a, b) As in Fig. 13a,b, but showing w (color) and (a) B (black contour) and mixing
24 ratio of cloud particles (blue contour) and (b) $g(\theta'_v/\theta_{v0})$ along the WSW-ENE segment
25 through C1 at 21:20 UTC 11 Jun 2012. (c, d) As in Figs. 14a,b, but showing w and (c) p'
26 (black contour) obtain from the relaxation method and $-(\partial p'/\partial z)/\rho_0$ (blue contour) and (d) p'_b
27 and its vertical PGF along the segment as in panels (a, b) at 21:20 UTC.

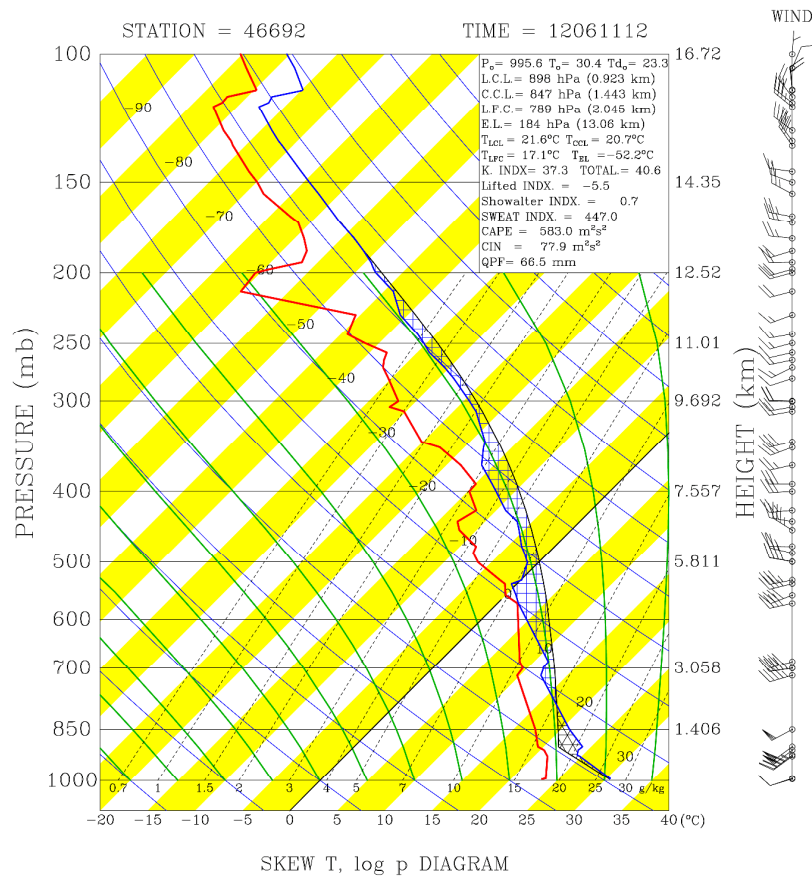


1 Figure 1. CWB surface analyses and positions of front/trough (or wind-shift line, thick dashed)
 2 at 850 (red), 700 (blue), 500 (green), and 200 hPa (orange) at 12:00 UTC 11 Jun 2012. The
 3 CReSS model domain is marked by the dotted box.

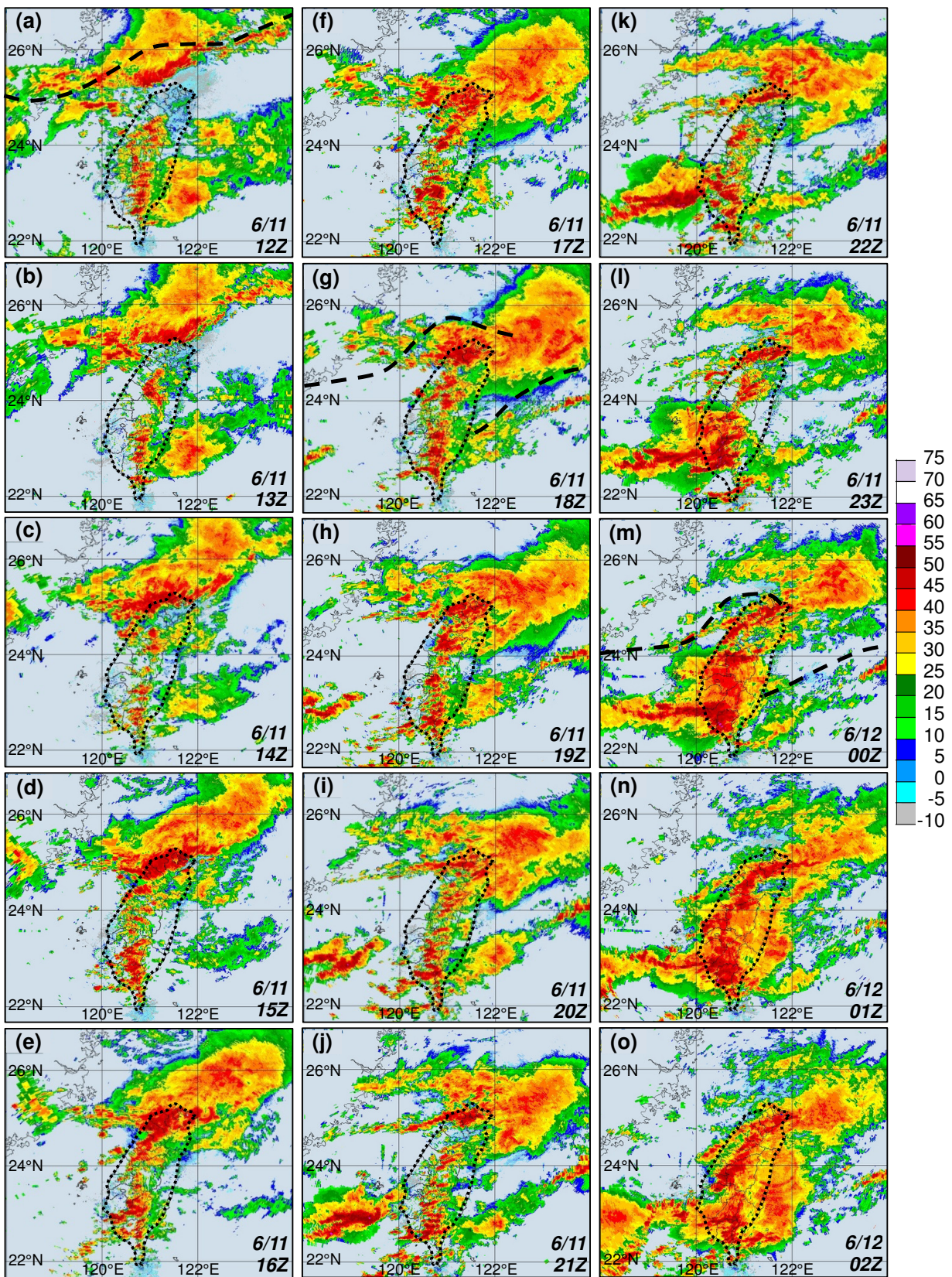


1 Figure 2. (a) NCEP (0.5°) 950 hPa analysis and (b) CReSS simulation of horizontal winds (m s^{-1} , speed shaded, scale to the right) at $z = 549$ m at 12:00 UTC 11 Jun 2012, with frontal
 2 position marked (thick dashed lines). (c, d) Frontal positions every 6 h from 06:00 UTC 11
 3

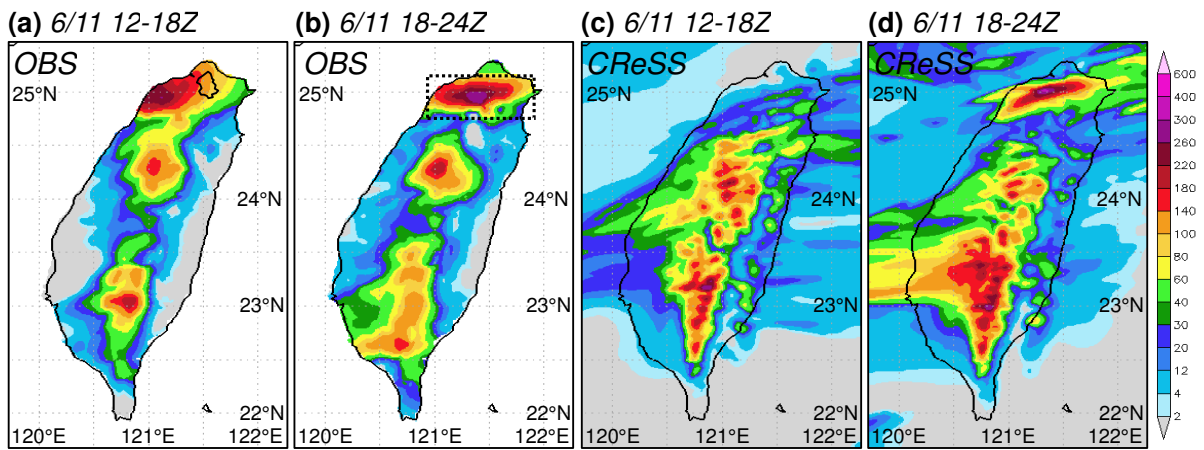
1 Jun to 12:00 UTC 12 Jun 2012 (c) at 950 hPa in NCEP analyses and (d) at $z = 549$ m in model
2 (see legend for line color and style), overlaid with topography (km, shading, scale to the right).
3 The triangle in (c) marks the location of Panchiao sounding in Fig. 3. (e, f) ASCAT oceanic
4 winds (m s^{-1}) near Taiwan at (e) 13:00 UTC 11 Jun and (f) 02:00 UTC 12 Jun, 2012, with
5 surface frontal position analyzed.



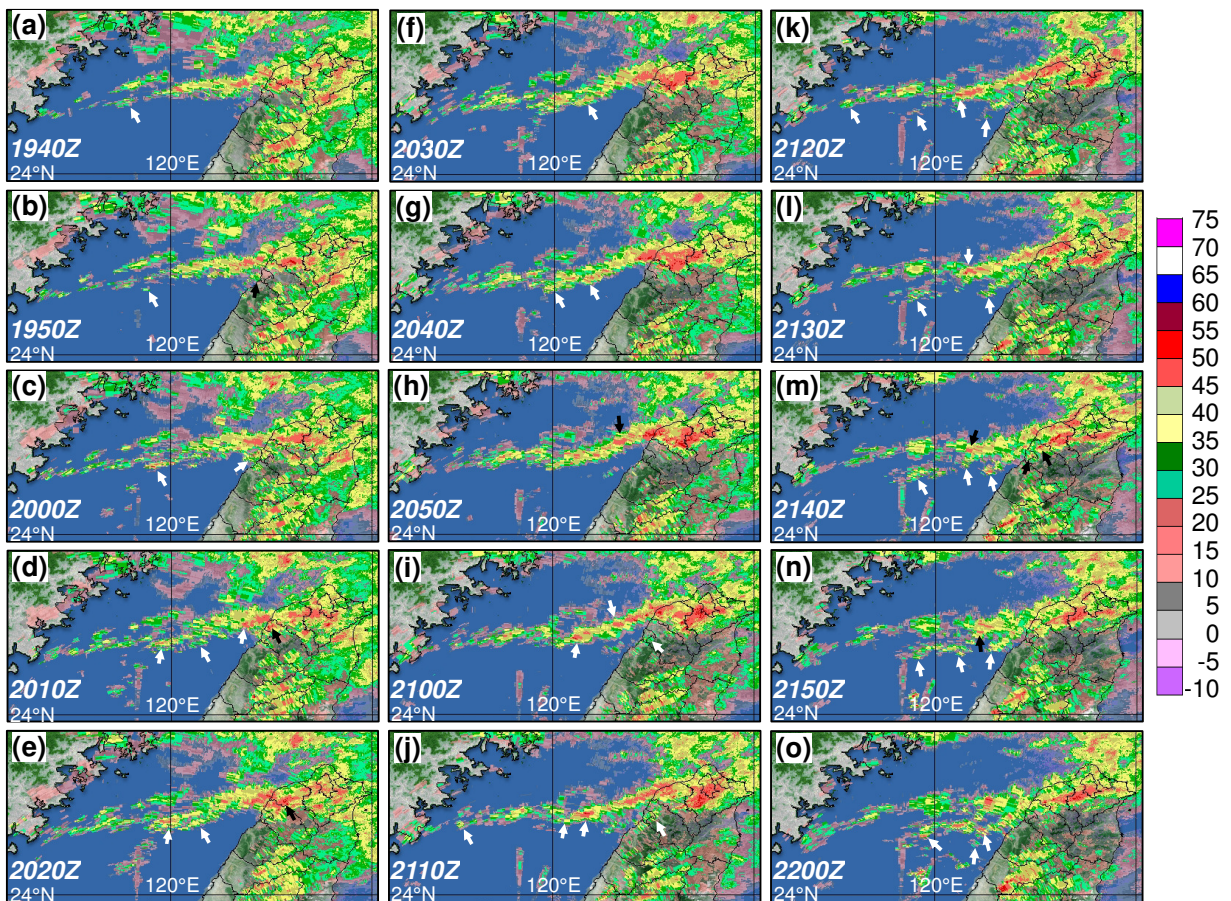
1 Figure 3. Thermodynamic (skew T -log p) diagram for the sounding taken at Panchiao (46692,
 2 cf. Fig. 2c for location) at 12:00 UTC 11 Jun 2012. For winds, full (half) barbs denote 10 (5)
 3 kts (1 kt = 0.5144 m s^{-1}), respectively.



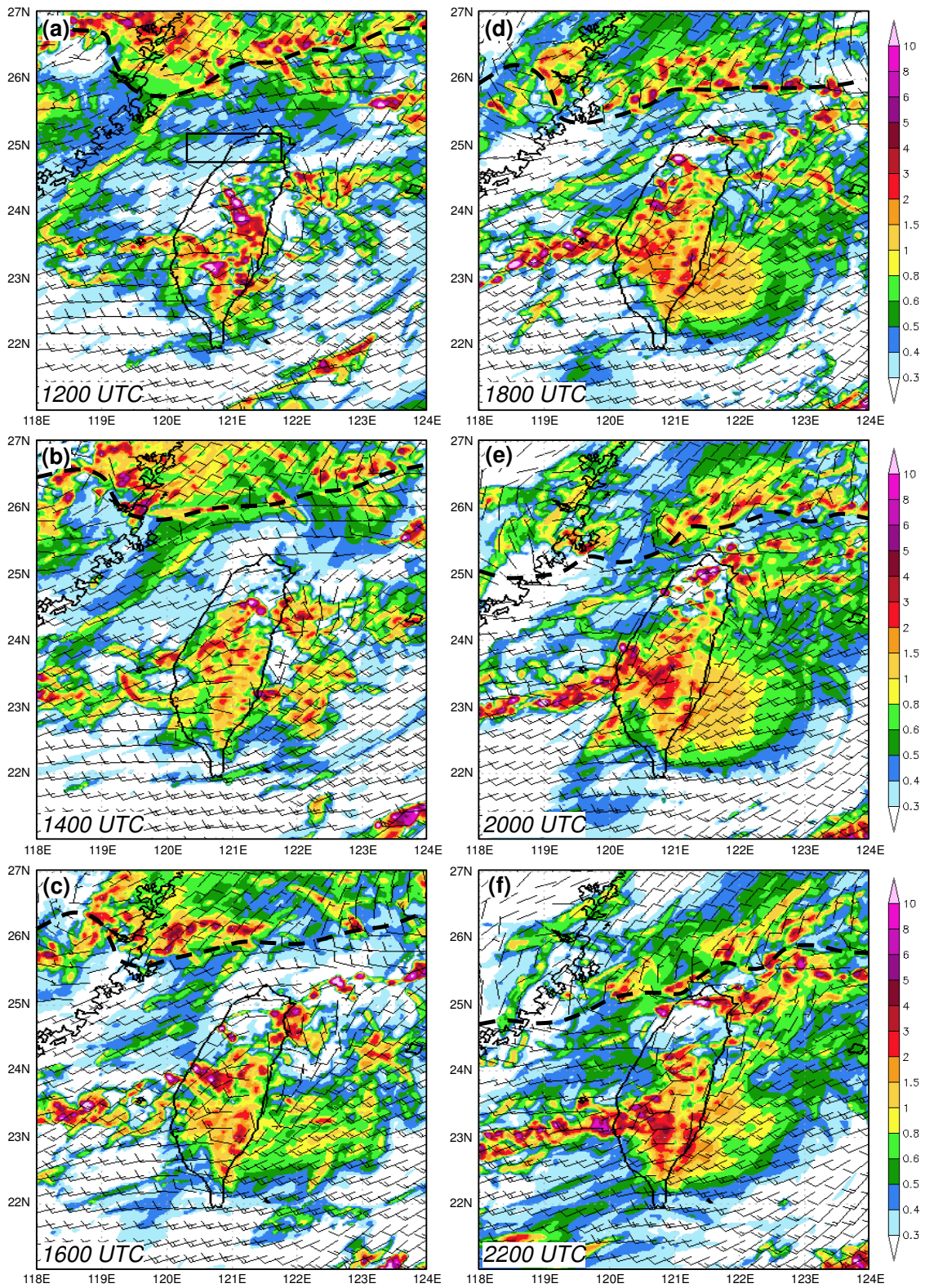
1 Figure 4. Composite VMI radar reflectivity (dBZ, color, scale to the right) over the Taiwan
2 area at 1-h intervals from (a) 1200 UTC 11 Jun to (i) 0200 UTC 12 Jun, 2012. The outline of
3 Taiwan is highlighted (thick dotted lines) and the surface frontal position is plotted at synoptic
4 times (thick dashed lines).



1 Figure 5. Distribution of observed 6-h accumulated rainfall (mm, color, scale to the right)
 2 over Taiwan during (a) 12:00-18:00 UTC and (b) 18:00-24:00 UTC 11 Jun 2012. The Taipei
 3 City boundary is depicted in panel (a), and the dotted box in (b) shows the region used in Fig.
 4 8 for rainfall average. (c, d) As in (a, b), but showing model-simulated rainfall over Taiwan
 5 and the surrounding oceans.

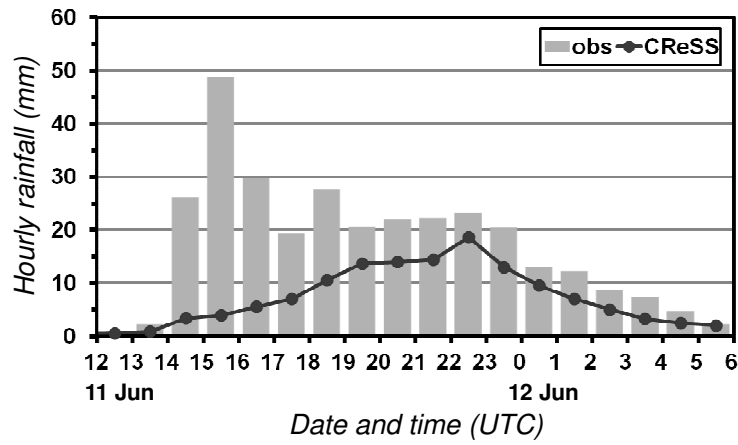


1 Figure 6. As in Fig. 4, but showing reflectivity over northern Taiwan and the upstream area
 2 every 10 min from (a) 19:40 UTC to (o) 22:00 UTC 11 Jun 2012 using a different set of
 3 colors. The arrows mark the initiation or strengthening of back-building cells, off the western
 4 end of a rainband or upstream from an old cell.

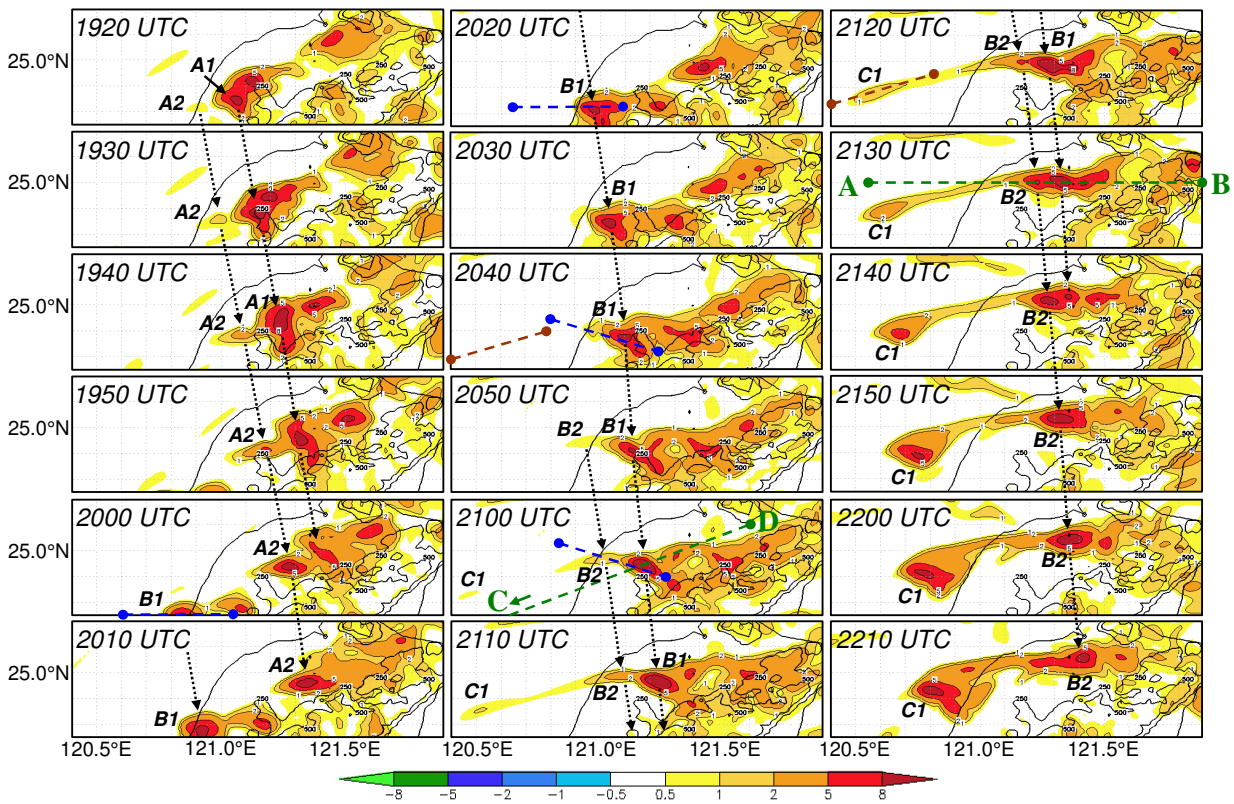


1 Figure 7. CRSS simulation of surface winds at 10 m height (m s^{-1}) and column-maximum
 2 mixing ratio of precipitation (rain + snow + graupel, g kg^{-1} , shading, scale to the right) every

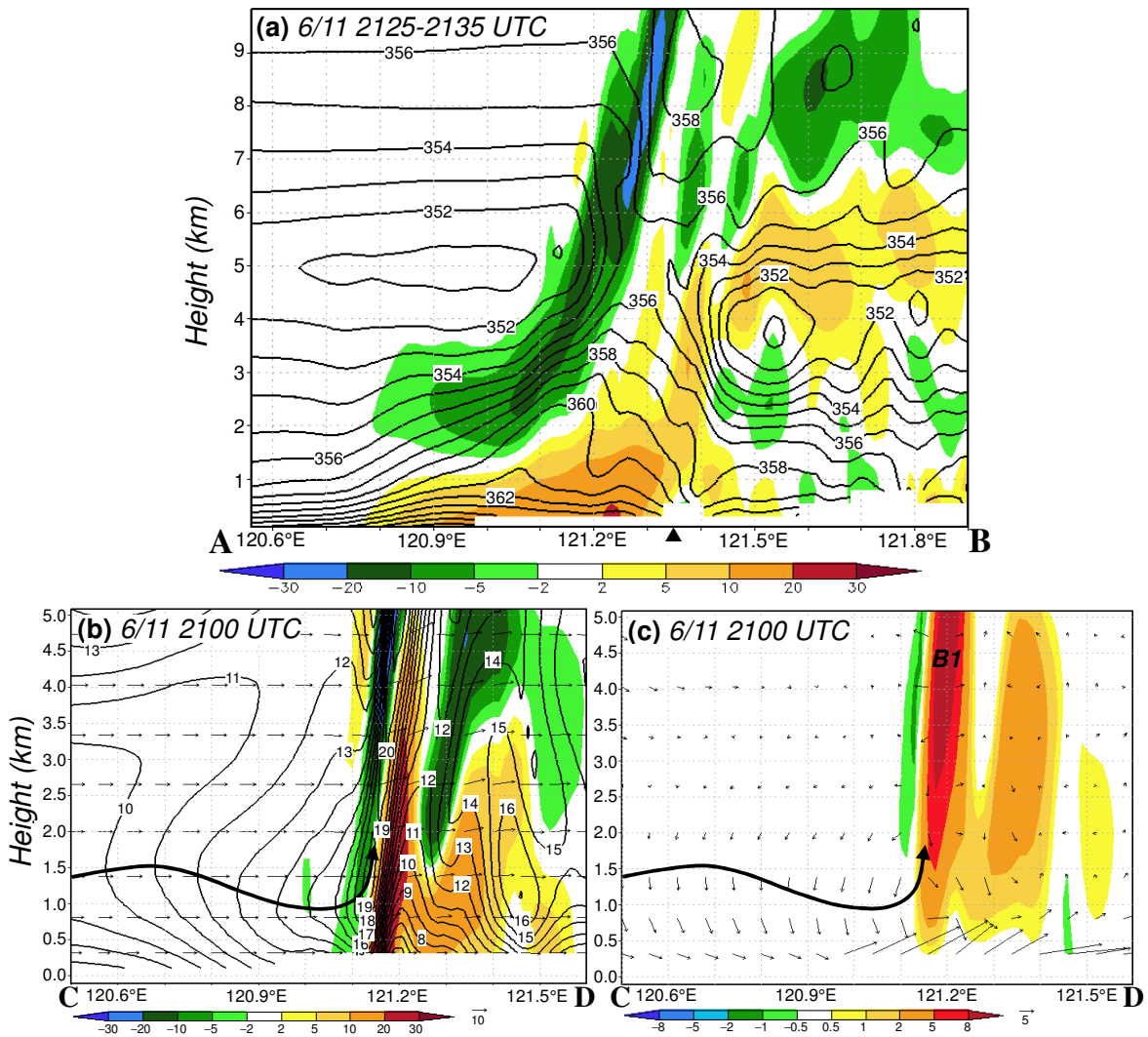
1 2 h from (a) 12:00 UTC to (f) 22:00 UTC 11 Jun 2012. For winds, full (half) barbs denote 10
2 (5) m s^{-1} , and the surface frontal positions are marked (thick dashed lines). The rectangle in
3 panel (a) depicts the area (24.75-25.15°N, 120.35-121.75°E) used for the separation method.



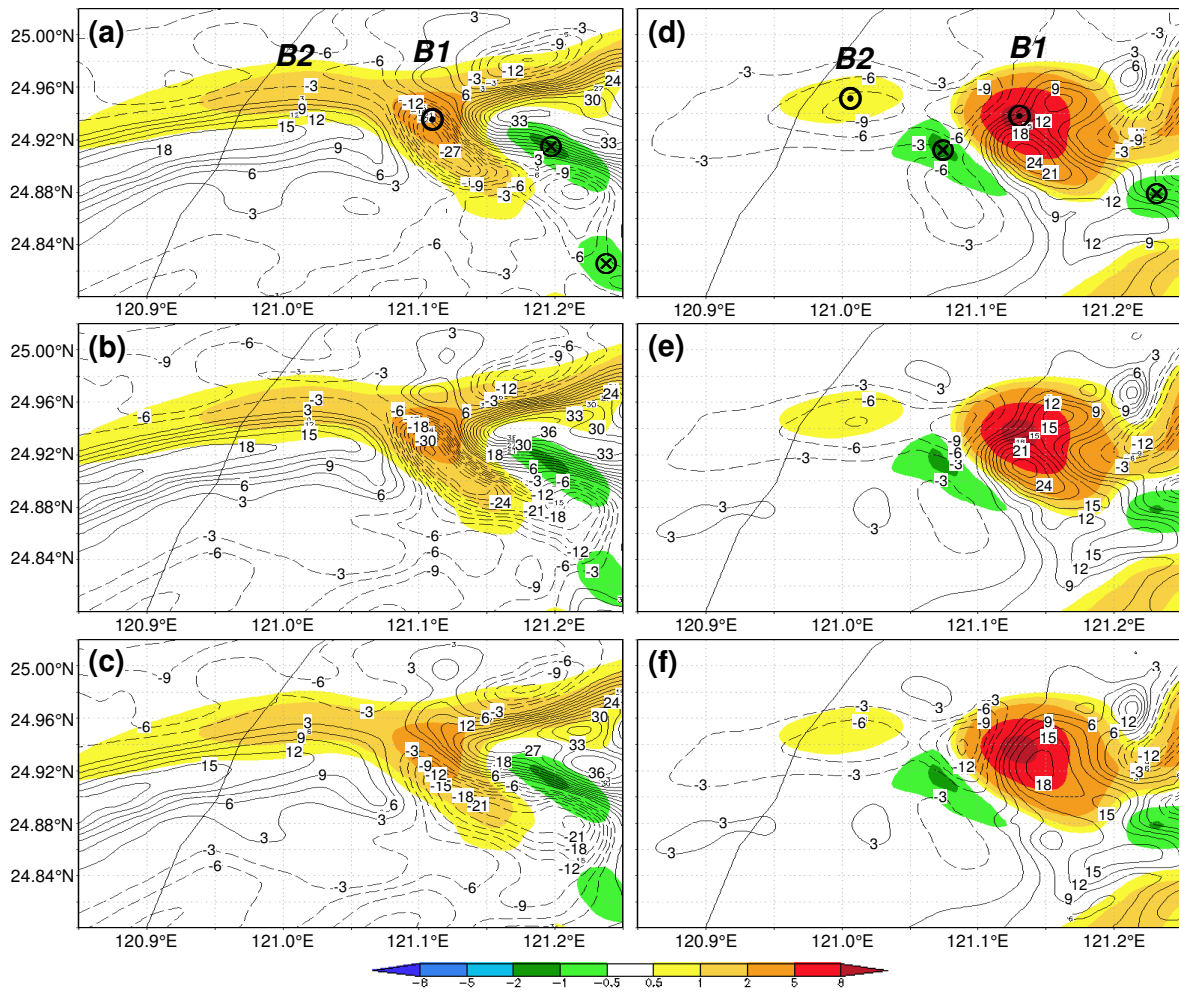
1 Figure 8. Time series of observed (gray bars) and simulated (curve with dots) hourly rainfall
 2 (mm), averaged inside the box shown in Fig. 5b (24.75-25.17°N, 120.87-121.85°E) over
 3 northern Taiwan from 12:00 UTC 11 Jun to 06:00 UTC 12 Jun 2012.



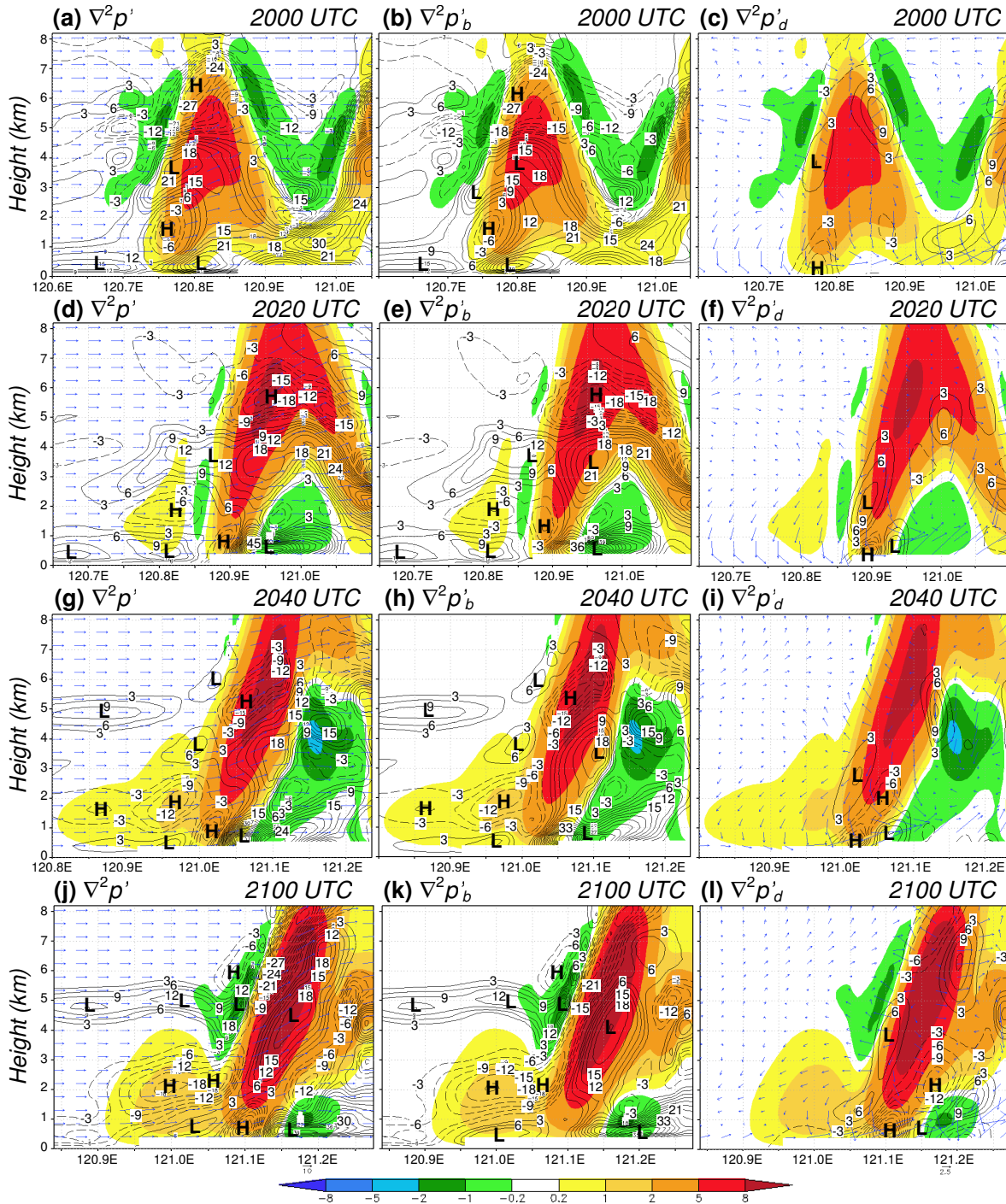
1 Figure 9. Model-simulated column-maximum vertical velocity (w , m s^{-1} , color and thin
 2 contours) every 10 min during 19:20-22:10 UTC 11 Jun 2012, overlaid with terrain elevation
 3 (m, thick contours at 250 and 500 m) in northern Taiwan. The color scale is shown at the
 4 bottom, and the contour at 0.5 m s^{-1} is not drawn. Old cells (A1, B1, and C1) and nearby new
 5 cells (A2, B2) of interests are labeled. Green dashed lines AB and CD depict the vertical
 6 cross-sections used in Fig. 10, and the short segments depict those used in Figs. 12-16 (blue
 7 (brown) ones through B1 (C1)).



1 Figure 10. (a) E-W vertical cross-section of model-simulated convergence/divergence (10^{-4}
 2 s^{-1} , color, positive for convergence) and θ_e (K, contour, every 1 K) along 25°N (line AB in Fig.
 3 9), averaged over 21:25-21:35 UTC 11 Jun 2012. The triangle marks the mean location of the
 4 updraft of B1. (b, c) As in panel (a), except showing (b) convergence/divergence (color) and
 5 wind vectors ($m s^{-1}$) and speed (isotach every 1 $m s^{-1}$) and (c) w ($m s^{-1}$, color) and vertical
 6 wind shear vector ($10^{-3} s^{-1}$, in cordinal direction, reference vectors both plotted) along the
 7 WSW-ENE section (line CD in Fig. 9) at 21:00 UTC 11 Jun 2012. Thick arrow-lines in (b, c)
 8 depict the axis of the LLJ.

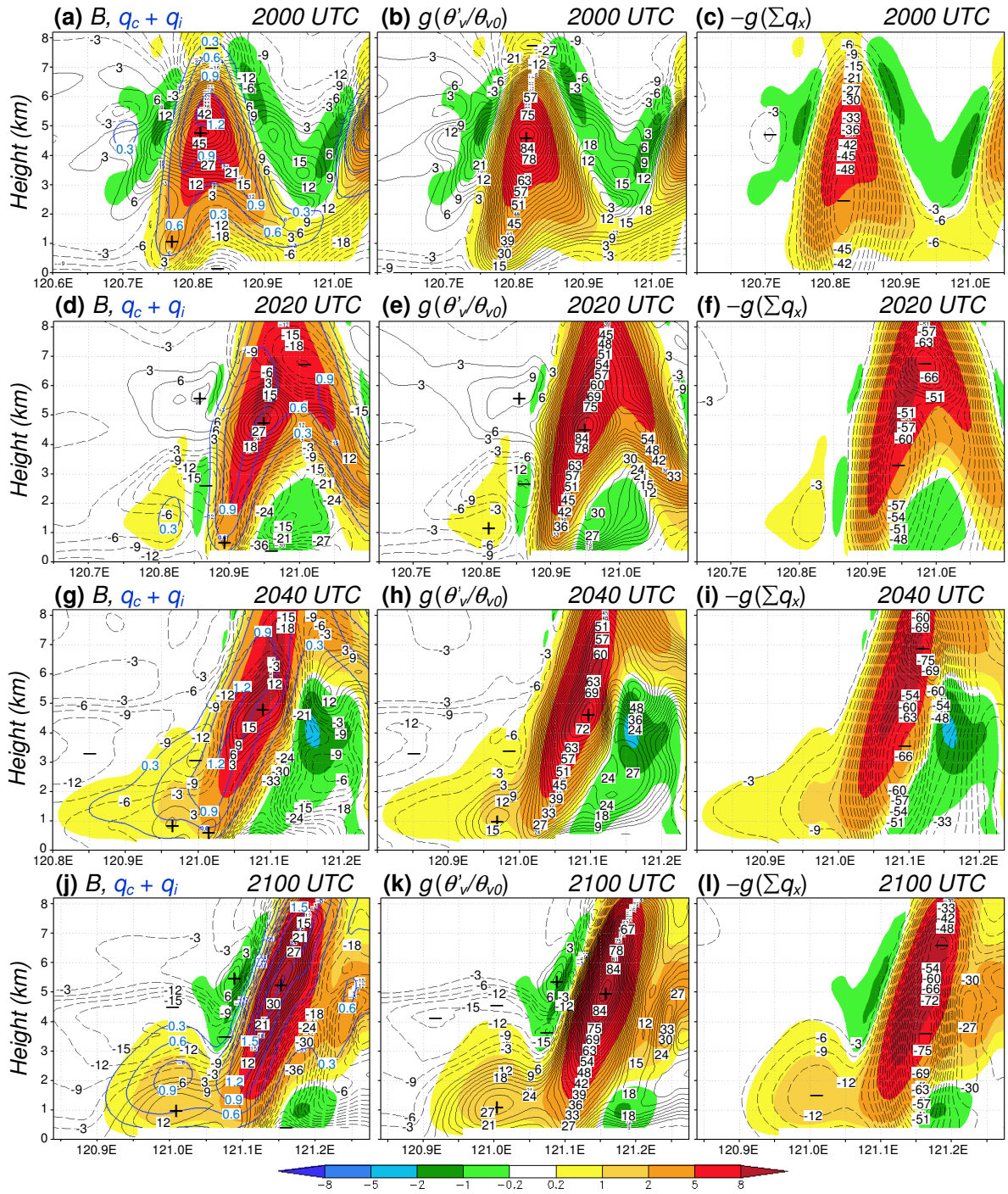


1 Figure 11. Model-simulated w (m s^{-1} , color, scale at bottom) and laplacian of perturbation
 2 pressure ($10^{-6} \text{ Pa m}^{-2}$, contour, every $3 \times 10^{-6} \text{ Pa m}^{-2}$, dashed for negative values) of cells B1
 3 and B2 at (left) 806 m and (right) 2929 m at 21:00 UTC 11 Jun 2012. (a, d) $\nabla^2 p'$ obtained
 4 from separation method, and (b, e) $\nabla^2 p' = \nabla^2 p'_b + \nabla^2 p'_d$ and (c, f) $\nabla^2 p'_b$ computed from Eqs.
 5 (3) and (4). Cells B1 and B2 and updraft and downdraft centers are labeled in panels (a) and
 6 (d).

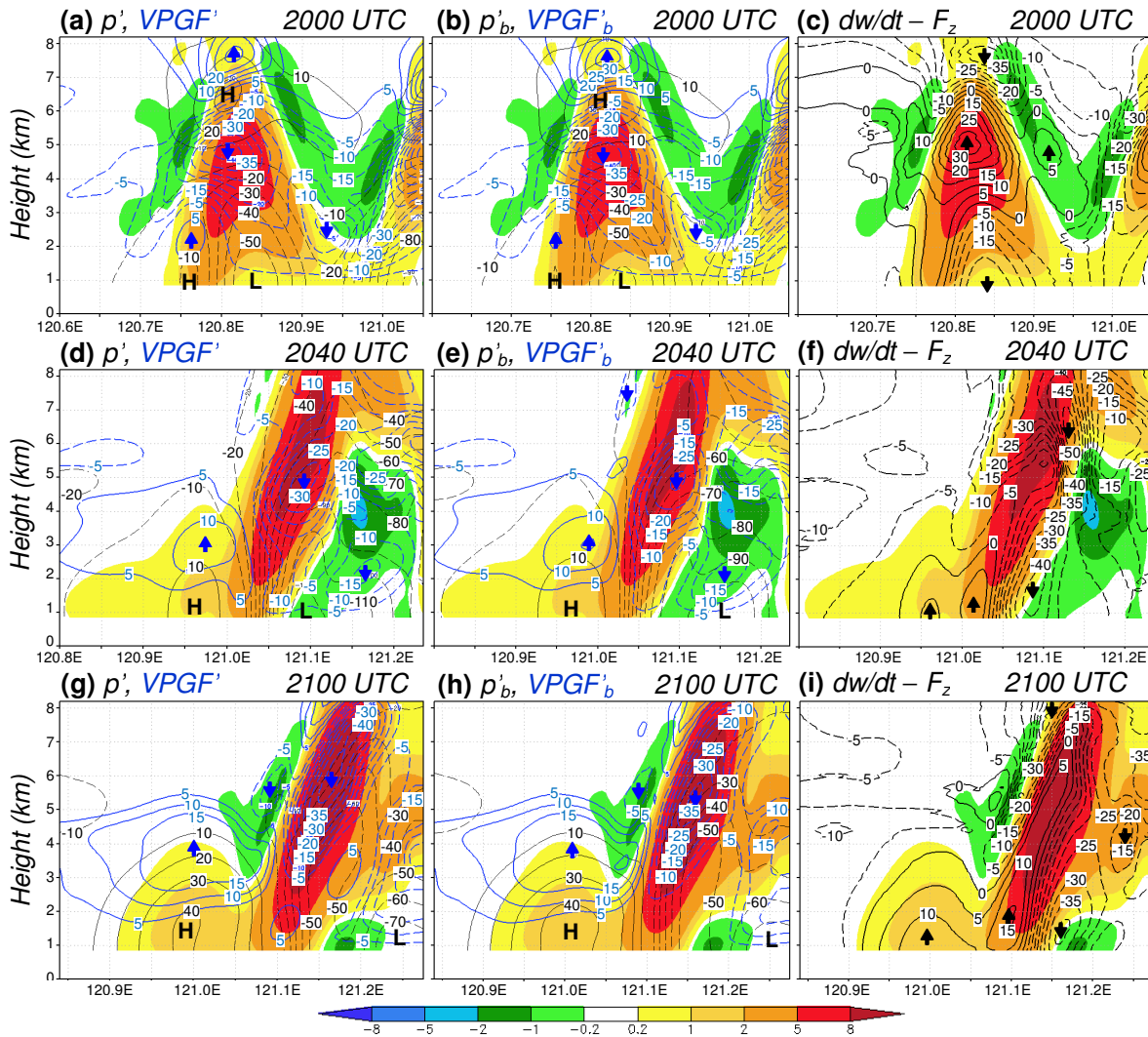


1 Figure 12. Vertical cross-sections of model-simulated w (m s^{-1} , color) and (a) $\nabla^2 p'$ (10^{-6} Pa
 2 m^{-2}) and wind vectors (m s^{-1} , reference vector at bottom) on section plain, (b) $\nabla^2 p'_b$
 3 (computed from Eq. 3), and (c) $\nabla^2 p'_d$ (computed from Eq. 4) and vertical wind shear vector
 4 (10^{-3} s^{-1} , in cardinal direction, reference vector at bottom) along the E-W segment through B1
 5 and B2 at 2000 UTC 11 Jun 2012 (cf. Fig. 9). All contour intervals are $3 \times 10^{-6} \text{ Pa m}^{-2}$ (zero

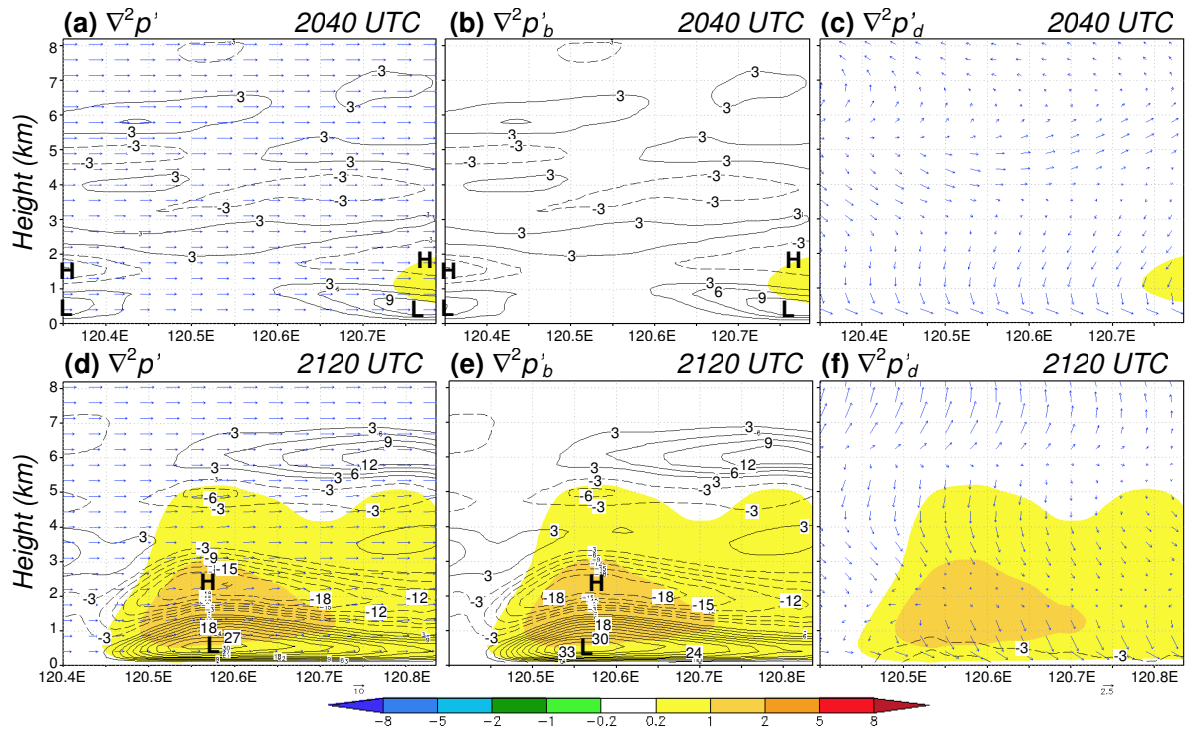
- 1 line omitted, dashed for negative values), and letters H (L) denote corresponding high (low)
- 2 pressure perturbations. (d-f), (g-i), and (j-l) As in (a-c), except at 20:20, 20:40, 21:00 UTC
- 3 (WNW-ESE segments for 20:40 and 21:00 UTC, cf. Fig. 9), respectively.



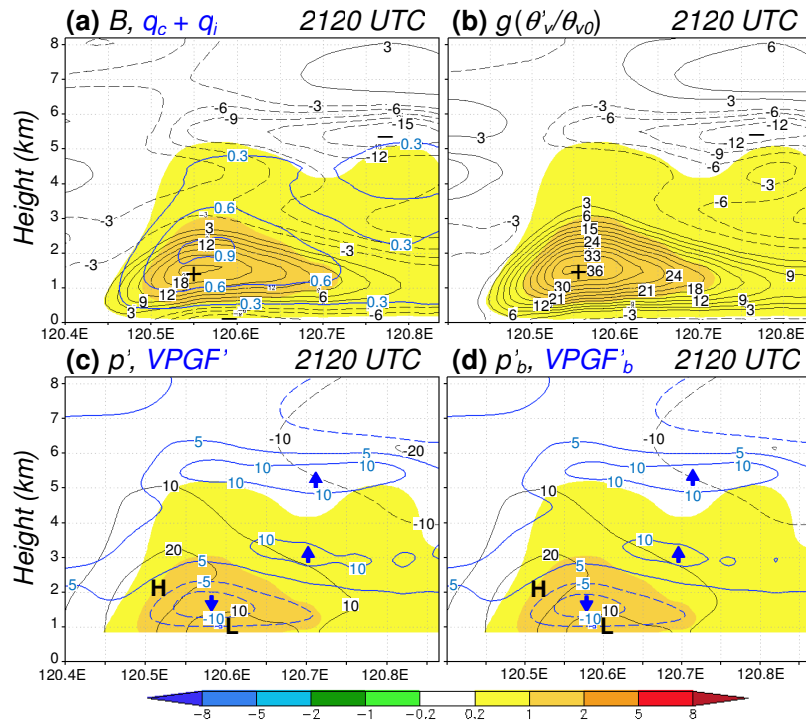
1 Figure 13. (a-c) As in Fig. 12a-c, but showing w and (a) buoyancy B (10^{-3} m s^{-2} , black
 2 contour) and mixing ratio of cloud particles (g kg^{-1} , blue contour, every 3 g kg^{-1}), (b)
 3 $g(\theta'_v/\theta_{v0})(10^{-3} \text{ m s}^{-2})$, and (c) $-g\Sigma q_x$ (10^{-3} m s^{-2}). All black contour intervals are $3 \times 10^{-6} \text{ Pa}$
 4 m^{-2} (dashed for negative values, zero line omitted), and + (-) signs denote upward
 5 (downward) maxima. (d-f), (g-i), and (j-l) As in (a-c), except at 20:20, 20:40, and 21:00 UTC,
 6 respectively.



1 Figure 14. As in Fig. 13, but showing w and (a, d, g) $p' = p'_b + p'_d$ (Pa, black contour, every
 2 10 Pa, dashed for negative values) obtained from the relaxation method and the corresponding
 3 perturbation PGF in the vertical ($-\partial p'/\partial z$), 10^{-3} m s^{-2} , blue contour), (b, e, h) p'_b (Pa) and
 4 its vertical PGF (10^{-3} m s^{-2}), and (c, f, i) dw/dt from vertical perturbation PGF and B (10^{-3} m
 5 s^{-2} , black contour). For force (per unit mass) and acceleration, all contour intervals are $5 \times$
 6 10^{-3} m s^{-2} (dashed for negative values), and upward (downward) arrows denote maxima
 7 (minima).



1 Figure 15. As in Fig. 12, but showing w (m s^{-1} , color) and (a) $\nabla^2 p'$ ($10^{-6} \text{ Pa m}^{-2}$) and wind
 2 vectors (m s^{-1}) on section plain, (b) $\nabla^2 p'_b$, and (c) $\nabla^2 p'_d$ and vertical wind shear vector (10^{-3}
 3 s^{-1} , in cardinal direction) along the WSW-ENE segment through C1 at 20:40 UTC 11 Jun
 4 2012 (cf. Fig. 9). (d-f) As in (a-c), except at 21:20 UTC.



1 Figure 16. (a, b) As in Fig. 13a,b, but showing w (color) and (a) B (black contour) and mixing
 2 ratio of cloud particles (blue contour) and (b) $g(\theta'_v/\theta_{v0})$ along the WSW-ENE segment
 3 through C1 at 21:20 UTC 11 Jun 2012. (c, d) As in Figs. 14a,b, but showing w and (c) p'
 4 (black contour) obtain from the relaxation method and $-(\partial p'/\partial z)/\rho_0$ (blue contour) and (d) p'_b
 5 and its vertical PGF along the segment as in panels (a, b) at 21:20 UTC.